NASA Technical Memorandum 100022

Contributions of Numerical Simulation Data Bases to the Physics, Modeling, and Measurement of Turbulence

Parviz Moin and Philippe R. Spalart

(NASA-TM-100022) CONTRIBUTIONS OF NUMERICAL SIMULATION DATA BASES TO THE PHYSICS, MODELING AND MEASUREMENT OF TURBULENCE (NASA) 33 p Avail: NTIS HC A03/MF A01 CSCL 01A G3/02

N87-29423

Unclas 0100125

September 1987

National Aeronautics and Space Administration

NASA Technical Memorandum 100022

Contributions of Numerical Simulation Data Bases to the Physics, Modeling, and Measurement of Turbulence

Parviz Moin and Philippe R. Spalart, Ames Research Center, Moffett Field, California

September 1987

National Aeronautics and
Space Administration

Ames Research Center
Moffett Field, California 94035

CONTRIBUTIONS OF NUMERICAL SIMULATION DATA BASES TO THE PHYSICS, MODELING, AND MEASUREMENT OF TURBULENCE[1]

PARVIZ MOIN
Department of Mechanical Engineering
Stanford University, Stanford, CA 94305
and NASA Ames Research Center, Moffett Field, CA 94035

PHILIPPE R. SPALART
Computational Fluid Dynamics Branch
NASA Ames Research Center, Moffett Field, CA 94035

1. Introduction

The use of simulation data bases for the detailed examination of turbulent flows has proved to be an effective research tool. In the past, studies of the structure of turbulence have been hampered by the limited number of probes and the impossibility of measuring all the desired quantities. Also, flow visualizations are confined to the observation of passive markers with limited field of view and contamination caused by time-history effects. Computed flow fields are a new resource for turbulence research, providing all the instantaneous flow variables in three-dimensional space. An essential part of the analysis of turbulence phenomena and the creation of physical models to describe them is a full account of all the velocity components and the pressure. Until now it has not been uncommon for the data on one velocity component to be extrapolated to model the behavior of all the velocity components and the vorticity vector. Numerical-simulation data bases permit analysis of the flow without any extrapolations from incomplete data. These data bases can also be used for the calibration of experimental measurement techniques, particularly in the near-wall region. As an example, the response of a hot-wire probe in a turbulent boundary layer will be computed.

Simulation data bases also provide much-needed information for phenomenological turbulence modeling. Even for simple shear flows, most of the terms in the Reynolds-stress transport equations have not been measured experimentally. To test a model for one of the terms in the transport equations, a model developer inserts the model into a computer code together with models for the other terms and makes an evaluation based on comparison of prominent quantities such as mean velocity profile or

[1]Some of the material in this paper was presented at the AIAA 25^{th} Aerospace Science Meeting, January 12-15, 1987, Reno, Nevada.

pressure coefficient with the experimental data. This is clearly an indirect method, and it can be misleading unless the models for the other terms are "correct". The test is much more informative if data for the quantity being modeled are available. Three-dimensional velocity and pressure fields from direct simulations can be used to compute all the terms in the transport equations for the Reynolds stresses and the dissipation rate. However only a few, geometrically-simple flows have been computed by direct numerical simulations, and the inventory of simulation fields does not fully address the current modeling needs in complex turbulent flows. Nevertheless, the available flow fields are sufficient for testing models in a number of important cases. These cases include turbulence near solid boundaries (flat or curved) where the available models are inadequate.

The availability of three-dimensional flow fields also poses challenges in developing new techniques for their analysis. Most current techniques do not take advantage of the vast amount of data at the researcher's disposal. They are often based on experimental methods, developed when limited data could be measured. Although some of these techniques are useful when comparing with experimental observations for code validation, new visualization and statistical techniques need to be developed to allow a comprehensive analysis of the simulation data.

In this paper we shall describe some of the techniques that have been used for the analysis of direct-simulation data bases in our studies of the mechanics of turbulent flows. We will use examples in which original contributions were made to the understanding of the physics of turbulent flows or to modeling efforts. These contributions have resulted from the availability of complete three-dimensional data.

In section 2 the computed *rms* values of wall-shear-stress fluctuations are compared with recent experimental data. In section 3, selected studies of the flow structures near the wall are presented. In section 4 it is shown that homogeneous turbulent shear flow is composed of organized structures similar to those in turbulent boundary layers. The application of statistical tools and of a stochastic-estimation algorithm to the identification of organized structures is discussed in section 5. The calibration of a hot-wire probe in a simulated boundary-layer flow field is presented in section 6. In section 7, the use of simulation data for phenomenological turbulence modeling is briefly discussed.

2. Code Verification and Issues Concerning Turbulence Statistics Near a Wall

Extensive comparison of the simulation results with experimental data is necessary to establish the physical realism of the simulated flow fields. The most comprehensive verification of large-eddy- and direct-simulation results has been in the fully-developed channel flow. This is in part due to the availability of a large set of measurements in this flow. Recently, a direct simulation of channel flow was performed with up to 4×10^6 grid points (Kim, Moin & Moser 1987). The Reynolds number based on the centerline mean velocity and channel half-width was 3300. All essential turbulence scales appear to have been resolved on the computational grid. The grid resolution ranged from $\Delta y^+ = 0.05$ in the vicinity of the wall to 4.4 at the channel centerline. The streamwise and spanwise grid resolutions were $\Delta x^+ = 12$ and $\Delta z^+ = 7$ respectively. The superscript $+$ indicates nondimensionalization in "wall units", using the

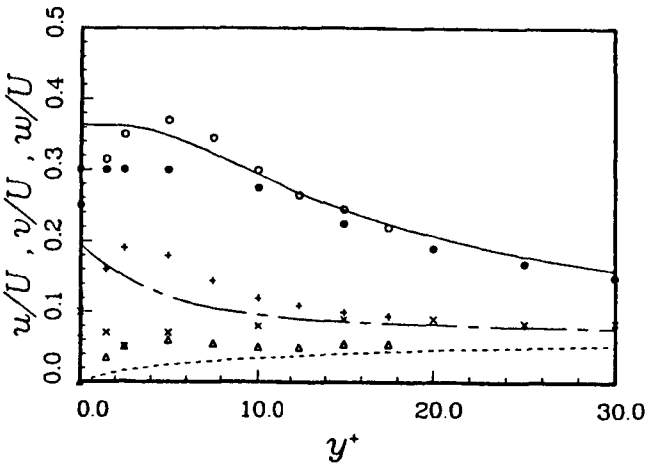

Figure 1. Turbulence intensities near the wall (normalized by the local mean velocity): —— u_{rms}/U, ---- v_{rms}/U, —·— w_{rms}/U; ○ u_{rms}/U, △ v_{rms}/U, + w_{rms}/U from Kreplin & Eckelmann (1979); • u_{rms}/U, × w_{rms}/U from Hanratty, Chorn & Hatziavramidis (1977).

shear velocity u_τ and the kinematic viscosity ν.

The results of this simulation have been extensively compared to the experimental data. In general, the agreement of various statistical correlations and instantaneous flow patterns with the data is good, but some discrepancies exist. Of particular interest is the limiting behavior of turbulent intensities near a wall. This behavior is related to the shear-stress and vorticity fluctuations, and the energy dissipation. By comparing the relative magnitudes of the *rms* streamwise-vorticity fluctuations at the wall (equal to $\overline{(\frac{\partial w}{\partial y})^2}^{1/2}$) and its peak value at $y^+ \approx 20$, Kim, Moin & Moser (1987) were able to draw conclusions about the vortical structures in the wall region. Here, u and w are the streamwise and spanwise velocity components, respectively. The wall value of the dissipation is

$$\epsilon_w = 2\nu\left[\overline{\left(\frac{\partial u}{\partial y}\right)^2} + \overline{\left(\frac{\partial w}{\partial y}\right)^2}\right]$$

Turbulent intensities, normalized by the local mean velocity, are plotted in Fig. 1. The general agreement between computed and measured profiles is good beyond the viscous sublayer ($y^+ > 10$). Very near the wall, large differences are discernible. In particular, the computed wall values of u_{rms}/U and w_{rms}/U are 0.36 and 0.20, respectively, whereas the experimental values for both quantities are about 30 to 50% lower (see Kreplin & Eckelmann 1979). Note that the values of *rms* wall-shear-stress fluctuations, normalized by the mean velocity gradient at the wall, are equal to the limiting wall values of the turbulent intensities normalized by the local mean velocity. Essentially identical values of wall-shear-stress fluctuations (0.36 and 0.19) were reported earlier by Moser & Moin (1984) from numerical simulation of a mildly-curved channel flow. Recent boundary-layer simulations by Spalart (1986) reveal that the intensities are weakly dependent on the Reynolds number. A fourfold increase in Reynolds number resulted in a 10% increase in the *rms* value of the streamwise shear-stress fluctuations at the wall.

Recently two experimental studies reexamined the previous measurements of wall-shear-stress fluctuations. Alfredsson, Johansson, Haritonidis & Eckelmann (1987) found that at the wall the *rms* streamwise fluctuating velocity gradient is about 0.40 times the mean value. They point out that heat loss to the probe substrate in flush-mounted probes causes a severe problem with air or oil as the flow medium, resulting in the low values reported previously. Although they did not directly measure the spanwise velocity gradient, they speculated, based on their findings for the streamwise component, that the *rms* spanwise velocity gradient is about $0.2\frac{\partial U}{\partial y}|_w$ in agreement with the results of simulations. Naqwi & Reynolds (1987) have also measured the wall-shear-stress fluctuations using a newly-developed laser wall-fan-fringe device. They reported an *rms* streamwise fluctuating velocity gradient of 0.38 times the mean value, which is again in good agreement with the simulation results. Their measurement of the spanwise component was not conclusive because they were unable to measure the spanwise velocity component sufficiently close to the wall. They report that the *rms* spanwise velocity gradient at the wall is greater than or equal to $0.13\frac{\partial U}{\partial y}|_w$.

This example is a case in which simulation results were used to critically examine laboratory measurements and were then confirmed by improved measurements. The quantities considered are of considerable importance in phenomenological and physical modeling of wall-bounded turbulent flows. The interaction which occured is an example of how computational and experimental studies complement each other.

3. Structure of Turbulence Near the Wall

The region near the wall in turbulent boundary layers is dominated by intermittent events that make large local contributions to turbulence production. A time trace of the streamwise component of the velocity at a point in the immediate vicinity of the wall ($y^+ = 0.4$) from a turbulent-channel-flow simulation is shown in Fig. 2. Large intermittent diversions from the mean value ($U^+ = 0.4$) are evident. Significant effort has been devoted to the detection of these (and other) events using conditional-sampling techniques and flow visualization. However, the organized structures or eddies that are associated with or cause such events have not yet been unequivocally identified. For example, using flow visualization, Kline, Reynolds, Schraub & Rundstadler (1967) observed that the low-speed streaks in the wall layer gradually lift up, oscillate, and break up leading to the bursting process with its large contribution to turbulence production. The focus of the research is the nature of the organized motions associated with regions of high Reynolds shear stress. Here, we will use the results of a direct turbulent-channel-flow simulation (Kim, Moin & Moser 1987) to address this question.

Contour plots of the three velocity components in a plane parallel to the wall (x, z) at $y^+ = 10$ are shown in Fig. 3. The patterns of the streamwise velocity component show the familiar elongated high- and low-speed streaky structures alternating in the spanwise direction. In contrast, the normal and spanwise velocity components do not exhibit streaky structures; rather they are dominated by small intermittent regions of intense fluctuations. In particular, most regions with a large normal velocity component are composed of sections with positive and negative values adjacent to each other. Of interest are the regions which make significant contributions to turbulence production, $-\overline{uv}\frac{\partial U}{\partial y}$. Contours of instantaneous uv in the same plane are shown in

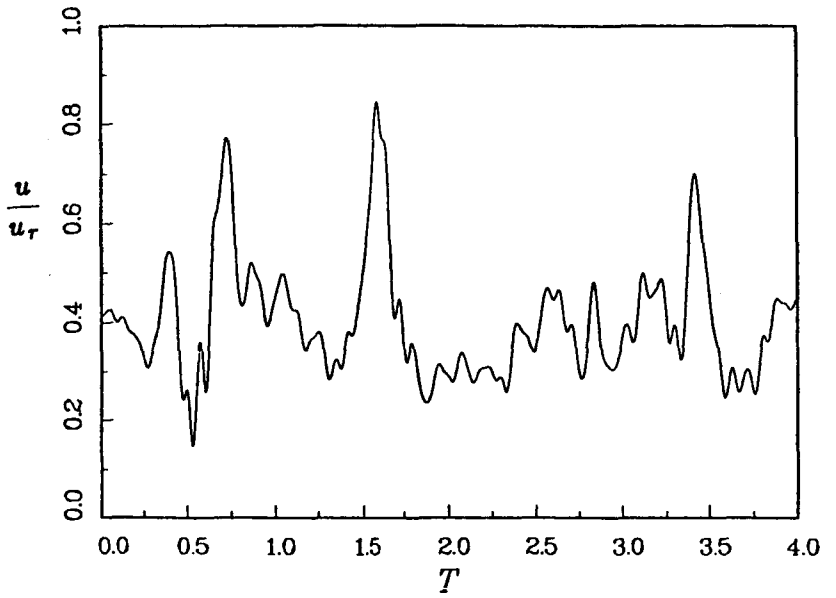

Figure 2. Time history of u/u_τ at $y^+ \approx 0.4$. The abscissa spans 6.4 δ/u_τ. The data was obtained from a channel-flow calculation at Reynolds number 1260 based on the mean centerline velocity and channel half-width.

Fig. 4. As expected from the contours of v, the uv patterns also show intermittent regions of intense fluctuations.

To examine the structures associated with regions of high turbulence production, vortex lines traced from the vicinity of the boxed areas in Fig. 4 are shown in Fig. 5. The vortex lines generally display horseshoe- (or hairpin-) shaped vortices. Two kinds of horseshoe vortices can be identified, those with the tip above the legs and downstream and others with the tip near the wall and upstream of the legs (inverted horseshoes). The induced velocity of the former structures is away from the wall (ejection), and the induced velocity of the inverted structures is toward the wall (sweep). The upright horseshoes have been conjectured to exist in turbulent boundary layers by numerous investigators starting with Theodorsen (1952), (see also Moin & Kim 1985). The existence of the inverted horseshoes in turbulent flows was first demonstrated using numerical-simulation data bases (Kim & Moin 1986a).

Two typical horseshoe-shaped structures (one of them from Fig. 5) are shown enlarged in Fig. 6. Note that in Fig. 6b only one of the legs of the horseshoe appears to have been formed from the convergence of vortex lines into a vortex rod, thus producing revolving fluid motion. The vortex lines near the other leg form a vortex sheet, rather than converge, and do not constitute a (revolving) vortical structure. Therefore, some of the horseshoe-shaped structures have only one identifiable vortex (leg) rather than a pair of counterrotating vortices. This observation is consistent with the contour plot of the normal velocity component in Fig. 3. In the plane shown, many of the regions of intense normal velocity are composed of a pair of negative and positive sections corresponding to a single vortex, and not a *triplet* as would be

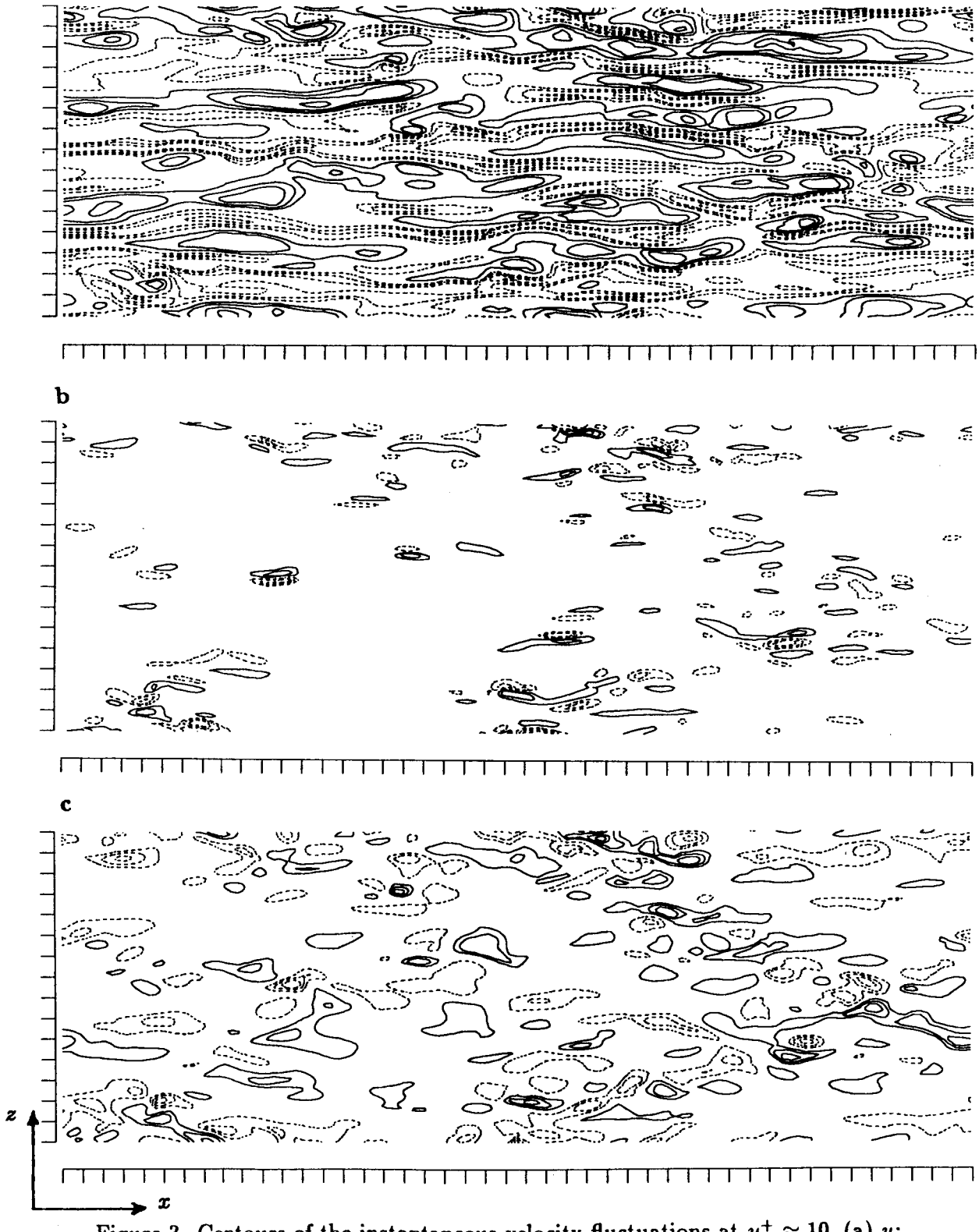

Figure 3. Contours of the instantaneous velocity fluctuations at $y^+ \approx 10$. (a) u; (b) v; (c) w. Dashed lines indicate negative contours. The streamwise extent of the figures is $2262\ \nu/u_\tau$, and the spanwise extent is $1131\ \nu/u_\tau$. In each figure, 10 contour levels are drawn spanning the maximum and minimum values of the quantity being plotted.

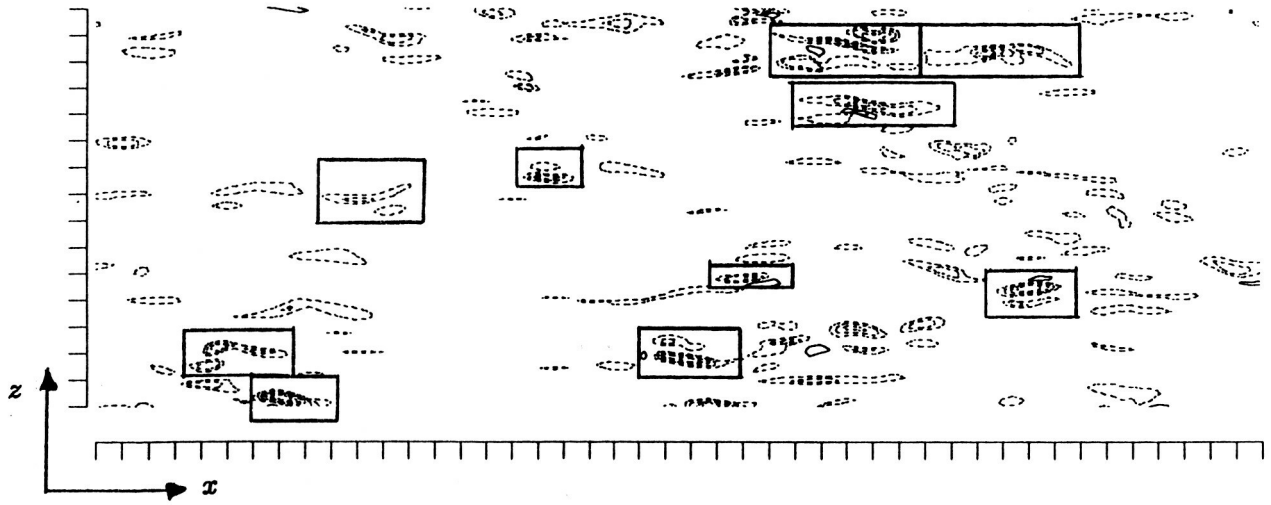

Figure 4. Contours of instantaneous uv. See caption of Fig. 3. The boxes mark some of the regions with intense shear stress.

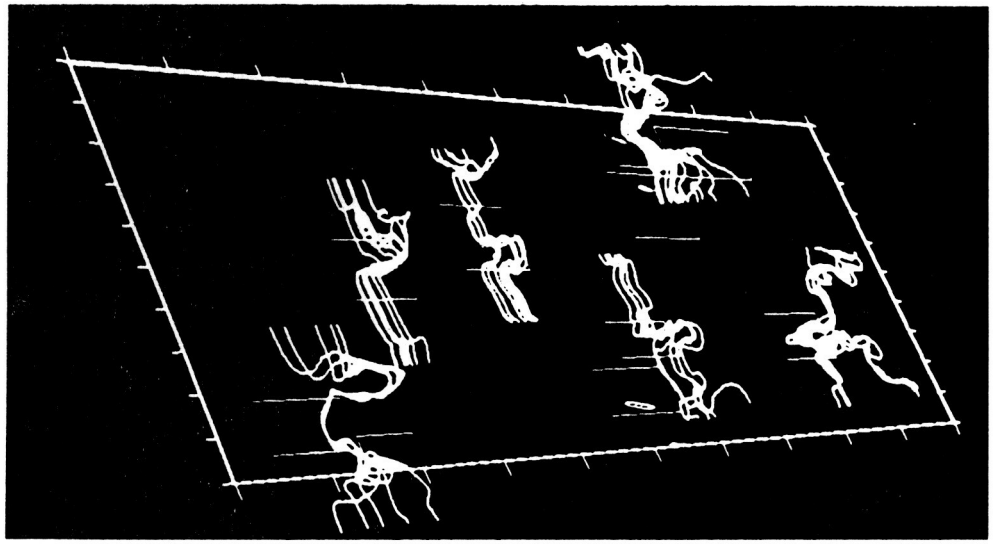

Figure 5. Vortex lines originating in the boxed areas of Fig. 4.

expected from a vortex pair. In fact in a random sampling of plots of velocity vectors projected onto (y, z) planes, normal to the flow direction, more solitary vortices than vortex pairs are observed. These vortices have a relatively short streamwise extent (100 to 200 wall units) and in all cases a region with high uv was located adjacent to one side of the vortex. These vortices were found to have long lifetimes, traveling downstream without losing their identity for at least several channel half-widths (see Moser & Moin 1984 and Kim & Moin 1986b).

Tracing vortex lines in three-dimensional space is an effective means of visualizing the vorticity field in a relatively small region of the flow. However, in turbulent

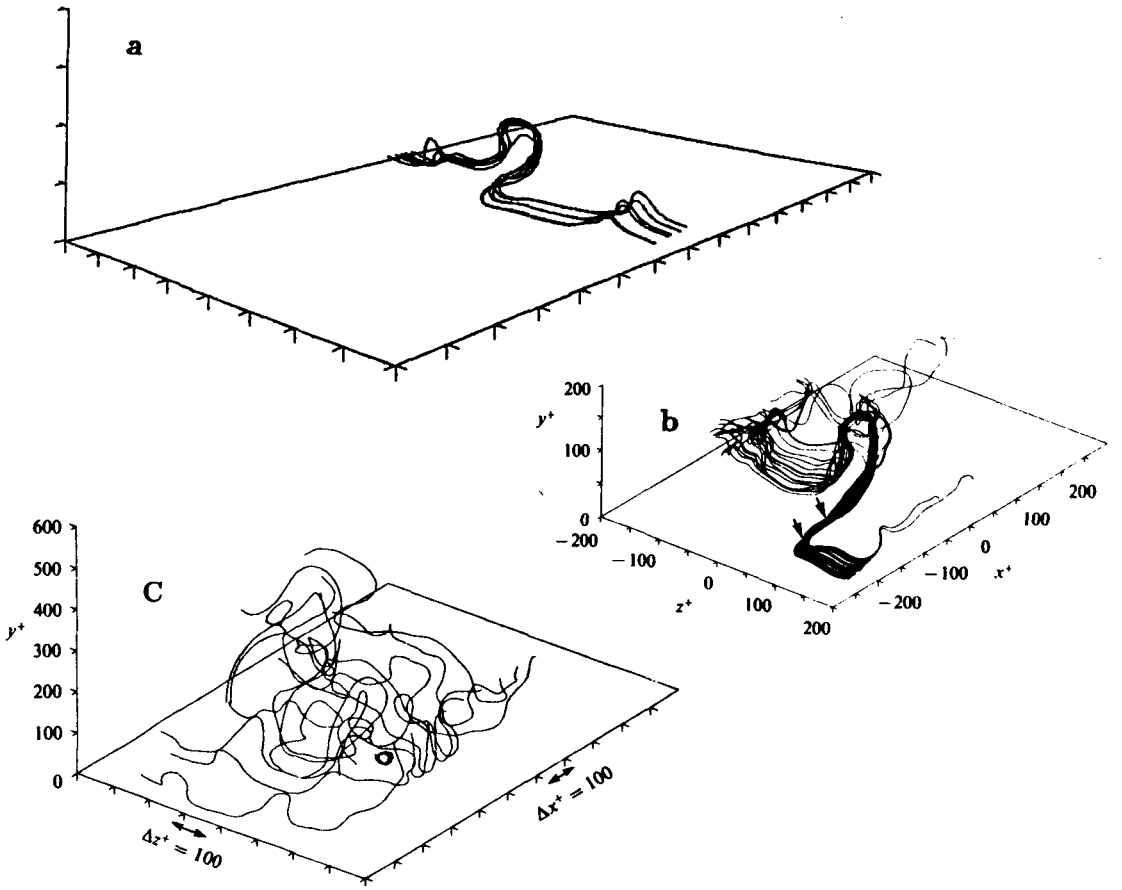

Figure 6. Vortex lines. a), b), displaying typical horseshoe- (or hairpin-) shaped vortical structure; c) randomly chosen.

flows, the random drawing of vortex lines can result in contorted pictures; see Fig. 6c. In general, one should select the regions for drawing vortex lines by a physical criterion. In the above example, we used contours of uv to aid in the selection of the trace starting points. Another disadvantage of vortex lines for flow visualization is that they indicate only the direction of the vorticity vector, not its magnitude. For example, it is difficult to identify a relatively weak vortex imbedded in a shear flow with large mean vorticity. Even if vortex lines are initialized within the core of the vortex, they will soon follow the direction of the mean shear rather than the vortex axis.

3.1 Skin-friction lines and pressure field near the wall

A patch of a turbulent boundary layer, with R_θ (the Reynolds number based on freestream velocity and momentum thickness) equal to 670, was explored in detail. The simulation is described by Spalart (1986). The size of the patch is about 550 by 235 wall units in the x and z directions, respectively. Figure 7 shows the skin-friction lines. Notice the large deviations of the shear-stress direction from the direction of the mean shear, and the strong convergence and divergence of the lines; positive and negative bifurcation lines can be identified (Hornung & Perry 1984).

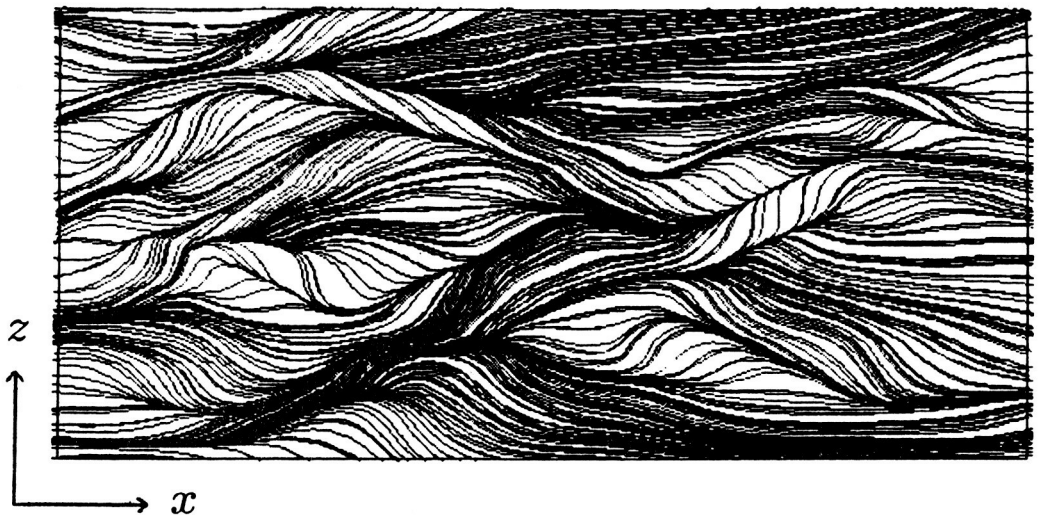

Figure 7. Skin-friction lines. The flow is from left to right.

Figure 8. Normal-velocity contours. $y^+ \approx 0.03$. —— positive, $v^+ = 0.002$, 0.006, 0.01; $\cdots$ negative, v^+ = -0.002, -0.006, -0.01.

Figure 8 shows the normal velocity component v^+ in a plane very near the wall. As expected, convergence of the skin-friction lines is associated with positive v^+, lift-up of near-wall fluid, and therefore "separation". Conversely, diverging friction lines indicate reattachment. In the continuity equation $u_x + v_y + w_z = 0$, it appears that large local values of v_y are often balanced by opposite values of w_z, rather than of u_x. Figure 9 shows contours of the streamwise vorticity in a plane in the buffer layer. The deviations of the friction lines in Fig. 7 are generally related to the high-vorticity regions seen in Fig. 9 (Perry & Hornung 1984), although the correlation is not as strong as with those of Fig. 8.

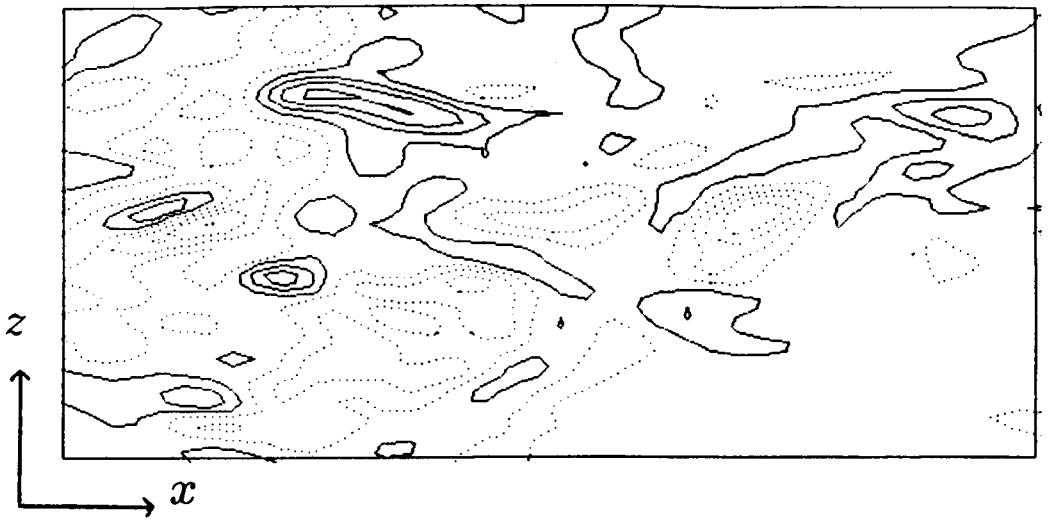

Figure 9. Streamwise-vorticity contours. $y^+ \approx 15$. —— positive, $\omega_x^+ = 0.2, 0.6, 1.$; ···· negative, $\omega_x^+ = -0.2, -0.6, -1$.

Figure 10. Wall-pressure contours. —— high pressure, $p^+ = 2, 6, 10$; ··· low pressure, $p^+ = -2, -6, -10$.

Figure 10 shows pressure contours at the wall and Fig. 11 shows pressure contours in three dimensions. The *rms* of p^+ at the wall is about 2.35; the skewness- and flatness factors are very moderate: about -0.04 and 4.25, respectively. At the wall, low pressure is strongly correlated with friction-line convergence, and high pressure with divergence. Also, elongated low-pressure regions are seen, whereas the high-pressure regions are more circular. These elongated regions are below the high-vorticity regions of Fig. 9. In Fig. 11a the low-pressure regions are again elongated. When comparing pressure and vorticity plots the low-pressure regions generally coincide with the cores of vortices. In contrast, the high-pressure regions in Fig. 11b are shaped more like

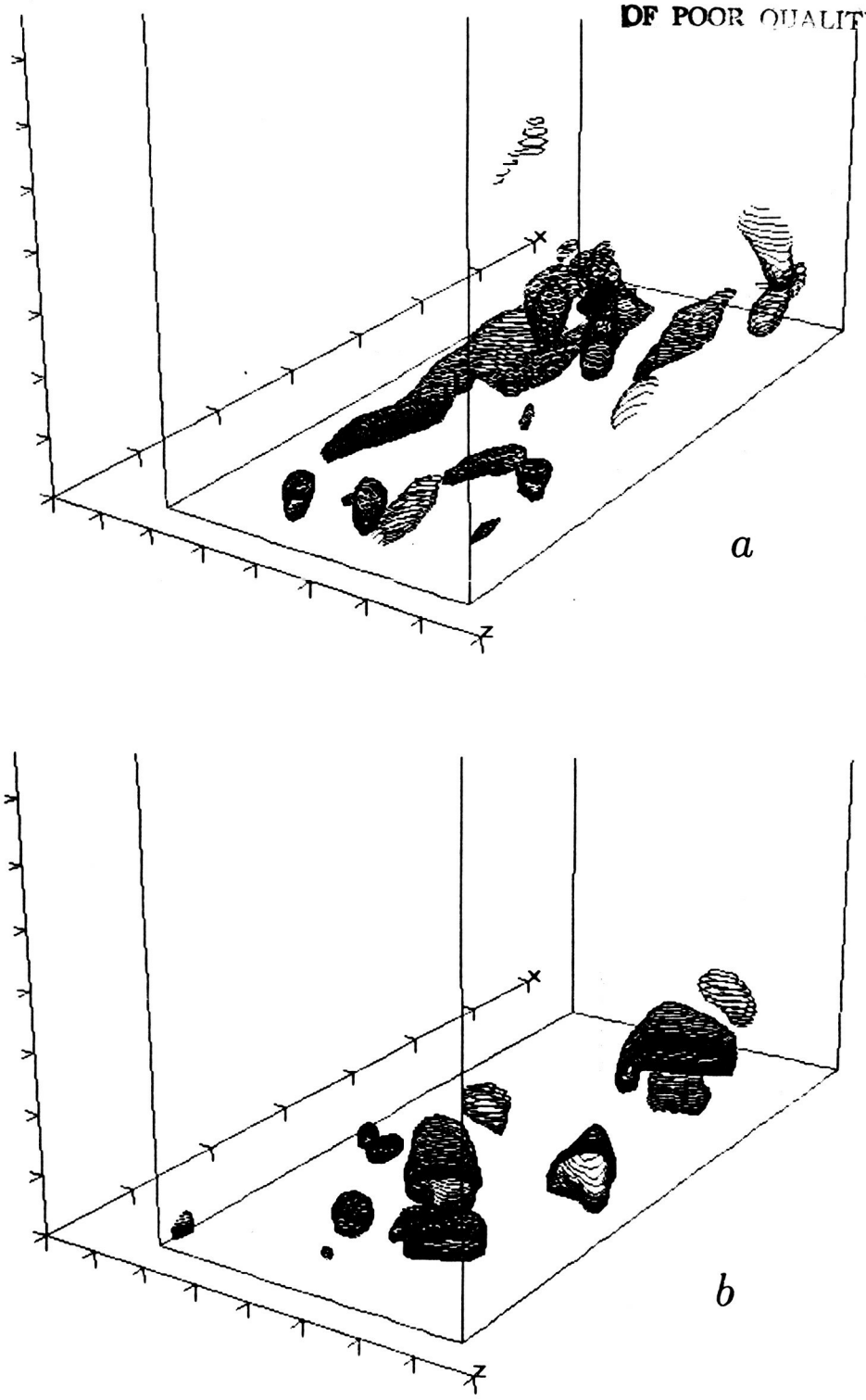

Figure 11. Three-dimensional pressure contours. (a) low pressure, $p^+ = -6$. (b) high pressure, $p^+ = +6$ (referred to the mean wall pressure).

hemispheres or columns. The high-pressure regions are strongly correlated in the normal direction, and hence with the outer-layer motions.

4. Organized Structures in Homogeneous Turbulent Shear Flow

One of the contributions of direct simulations has been the demonstration of the existence of organized structures in homogeneous flows similar to those found in turbulent boundary layers and mixing layers. These findings reaffirm the relevance of homogeneous "building-block flows" and of their detailed study en route to understanding more complex flows.

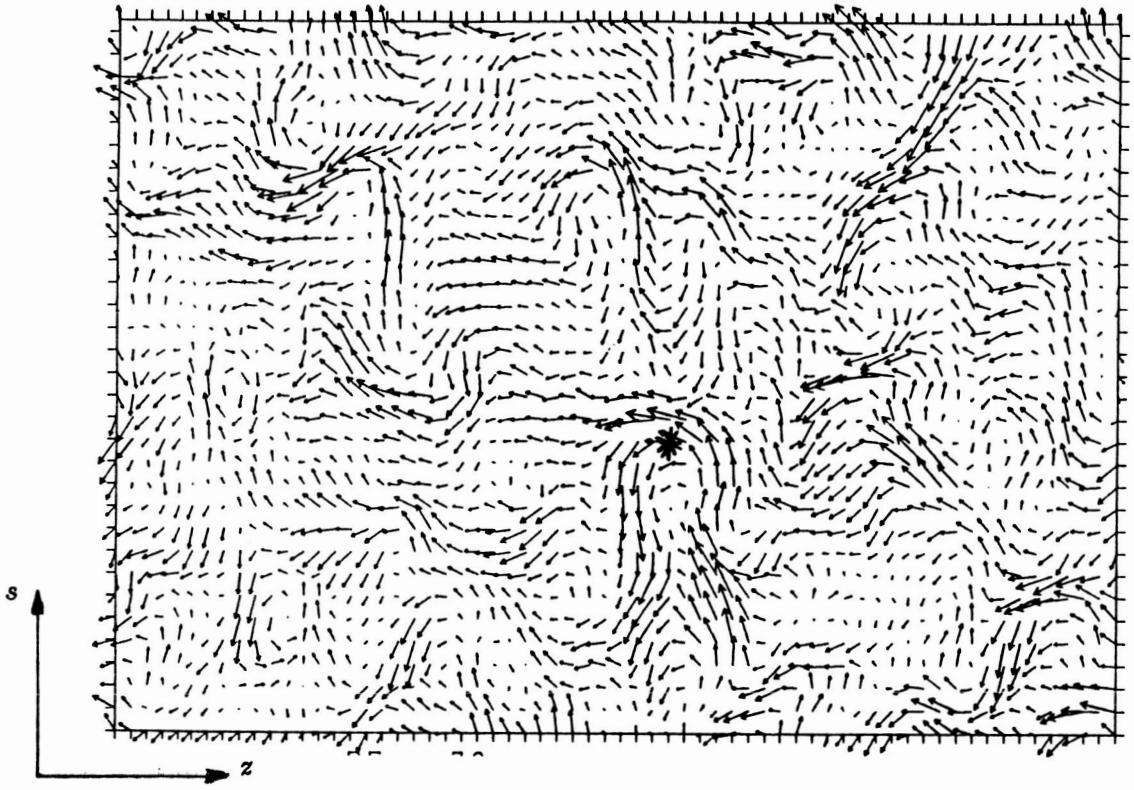

Figure 12. Projection of instantaneous vorticity vectors on a plane inclined at 45° to the flow direction. Tick marks represent the locations of the computational grid.

Rogers & Moin (1987) found that hairpin- or horseshoe-type vortices are generated from mean vorticity in homogeneous shear flow. They concluded that such vortices are not peculiar to turbulent boundary layers; they are present in all shear flows. The calculation was started from an initially-random velocity field with a prescribed energy spectrum. At the early stages of the flow development, the vortices are aligned with the expansive principal axis of the mean strain-rate tensor of the imposed shear. Eventually the rotation component of the mean shear reduces the inclination angle of these vortices and also causes the development of strong coherent spanwise vortex filaments. The projection of vorticity vectors onto a plane inclined at 45° to the flow

direction is shown in Fig. 12. Organized vortical structures, many of them hairpin-shaped, are clearly discernible. In this study, it was also shown that the structures of the Reynolds-stress tensor and heat-flux vector are very similar to those in the outer regions of turbulent boundary layers. We believe that this similarity in statistical parameters is due to the dominance of identical organized structures (hairpins) in both flows.

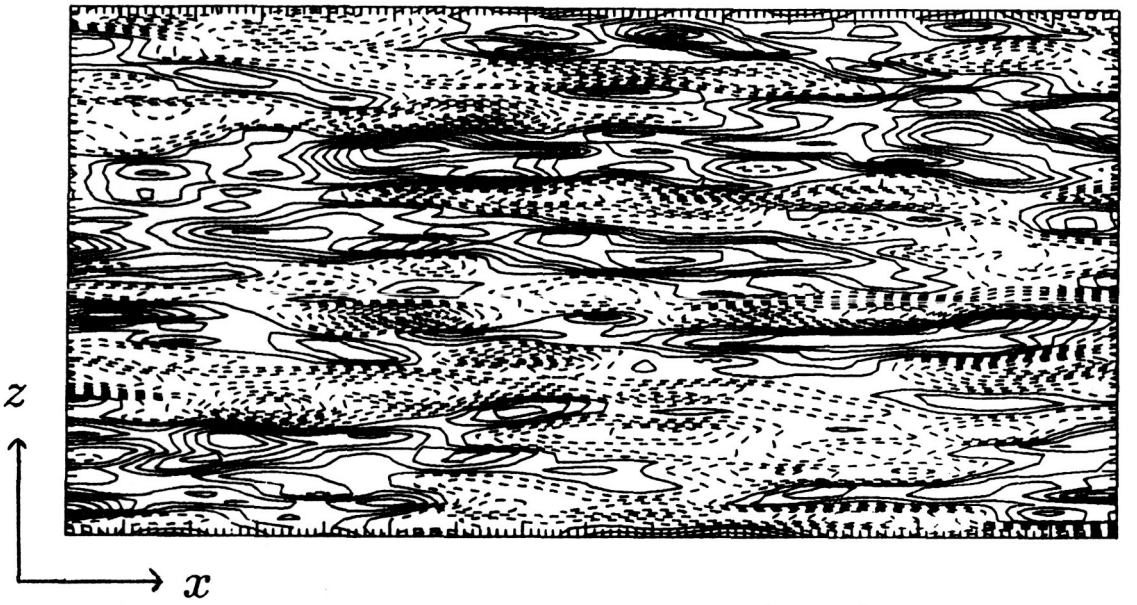

Figure 13. Contours of the instantaneous velocity fluctuations in homogeneous turbulence with high shear rate. Dashed lines indicate negative contours.

In Rogers & Moin's simulations, we did not detect any similarity between the contours of the velocity fluctuations in the homogeneous-shear-flow calculations and those in the wall region of turbulent channel flow (Fig. 3). In particular, the streaky patterns in the streamwise component of the velocity near the wall were absent in the homogeneous flow field. It was conjectured that the presence of a *strong* mean shear in the channel causes the formation of streaks. Lee, Kim & Moin (1986) simulated a homogeneous shear flow with a nondimensional shear parameter, Sq^2/ϵ, comparable to that in the wall region of turbulent channel flow. Here S is the shear rate and q^2 and ϵ are the turbulent kinetic energy and dissipation rate, respectively. The velocity contours from these simulations (Fig. 13) are strikingly similar to those in Fig. 3. Moreover, the structure of the Reynolds-stress tensor and several other non-dimensional statistical parameters are in good agreement with those in the near-wall region of turbulent channel flow. Again, the similarity of the organized structures in both flows leads to statistical similarity as well.

5. Statistical Analysis of Organized Structures

Methods based on long-time averaged correlations have been largely abandoned in studies of the structure of turbulence since it is generally believed that time-averaging suppresses information on the underlying time-dependent flow structures. Instead, conditional or phase-averaging techniques have been adopted which describe the average behavior of the velocity field in the neighborhood of points where conditions (or data) about the field are given. It will be shown in section 5.2 that *conditional eddies can be obtained, to a first-order approximation, from the time-averaged two-point correlations.* The advantage of statistical techniques for the study of coherent structures is that a large number of flow realizations are taken into account, which reduces the influence of the user's prejudices and the risk of detecting rare, nonrepresentative events. These techniques also provide quantitative information about the flow structures. Their main disadvantage is their imposition of artificial symmetries and the effect of jitter or smearing on the shape of the averaged structure. This effect is especially pronounced if the flow is not dominated by a single kind of structure occurring randomly in space, but by several equally important kinds of structures. The jitter problem is not peculiar to long-time averaged statistics; it is also present in conditional averaging. The jitter can be reduced by increasing the number of conditions at a point or prescribing conditions at more that one point; however this also reduces the statistical sample.

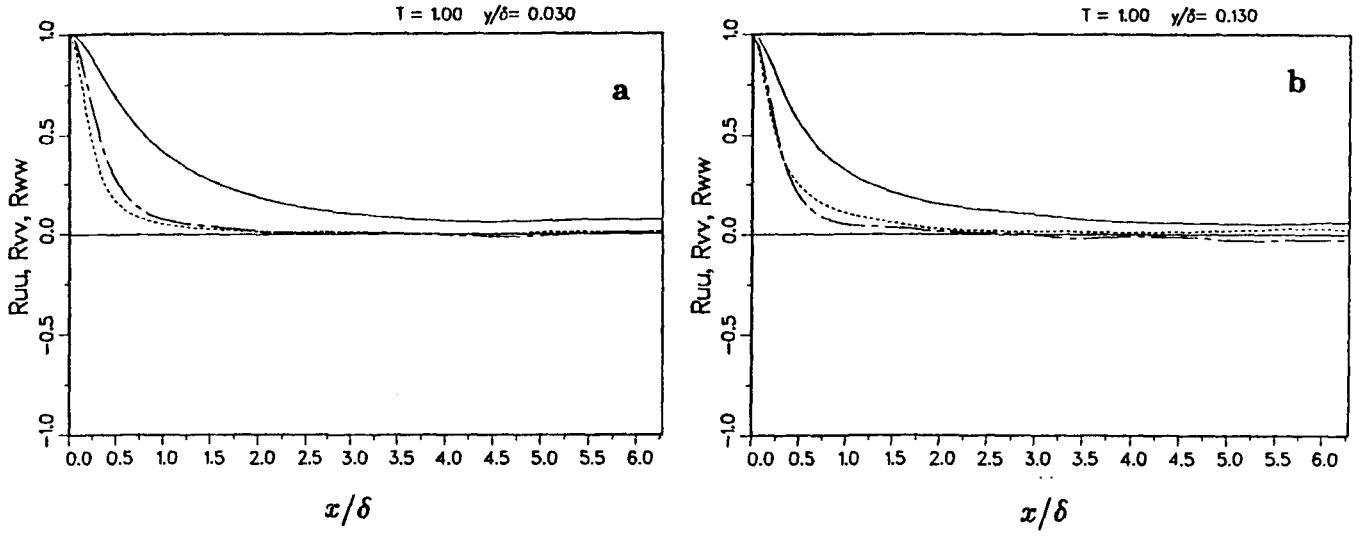

Figure 14. Two-point correlations with separations in the streamwise, x, direction. —— R_{uu}, ---- R_{vv}, —·— R_{ww}. (a) $y/\delta = 0.03$, $y^+ = 5.4$; (b) $y^+ = 23$.

In our studies of the structure of wall-layer turbulence, long-term statistical correlations have played an important role (Moin & Kim 1982, 1985). Higher-order statistical correlations have been used to examine the flow structures and to establish whether the observed structures occur frequently. In particular, we have used two-point velocity and vorticity correlations to infer the form of coherent structures

in shear flows and to obtain their averaged length scales. In examining two-point correlation profiles, the value of the information is highly dependent on the direction of 'probe' separation. It is much more informative to obtain two-point correlation functions with the direction of probe separation along the eddy axis rather than along the Cartesian coordinate axes. In Moin & Kim (1985), vorticity and velocity correlations with the probe separation along lines inclined to the flow direction were used to demonstrate the existence of inclined vortical structures.

Two-point correlations of the velocity components with streamwise and spanwise separations are shown in Figs. 14 and 15, respectively. In the wall region, it can be seen that the streamwise-velocity correlation shows significant elongation, consistent with the existence of streaks and with Fig. 3a. The normal- and spanwise-velocity correlations do not show nearly as large a streamwise elongation. This is also consistent with the velocity patterns shown in Fig. 3. Near the wall, all correlations in the spanwise directions have negative minima. In particular, the location of the negative minimum in $R_{uu}(r_z)$ is at $z^+ \approx 50$ corresponding to the mean spacing of the low- and high-speed streaks of 100 wall units as observed experimentally. The correlation R_{vv} has a sharp minimum consistent with the adjacent positive and negative regions shown in Fig. 3. The negative minimum of R_{vv} persists at larger y values, albeit at somewhat larger r_z's. However, R_{ww} does not have a negative minimum beyond $y^+ = 18$. The absence of a minimum in R_{ww} implies that vortex *pairs* are not a dominant feature of near-wall turbulence, although the patterns shown in Fig. 3 do not rule out the presence of vortex pairs. The existence of solitary vortices discussed in conjunction with Fig. 3 are consistent with the behavior of $R_{vv}(z)$ in Fig. 15 and with normal two-point correlations, $R_{ww}(y, y')$ (Moin & Kim 1985).

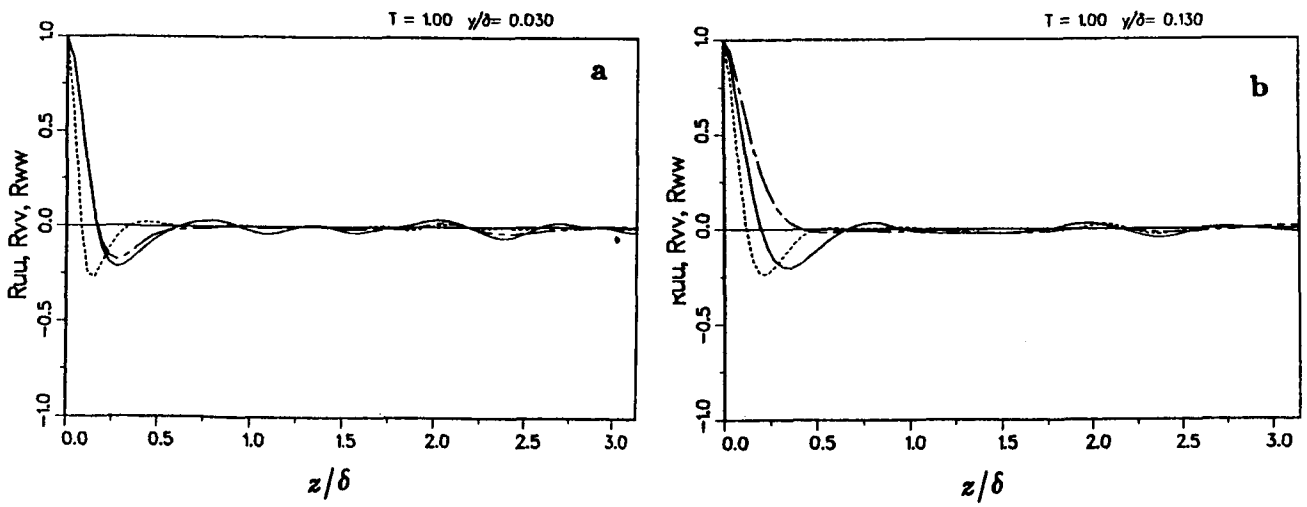

Figure 15. Two-point correlations with separations in the spanwise, z, direction. —— R_{uu}, ---- R_{vv}, —·— R_{ww}. (a) $y/\delta = 0.03$, $y^+ = 5.4$; (b) $y^+ = 23$.

Two-point correlation data have also been used to identify energetic structures in the wall layer. The characteristic-eddy decomposition (Lumley 1967) was applied to

both large-eddy-simulation data (Moin 1984) and direct-simulation data in turbulent channel flow. One of the attractions of the characteristic-eddy decomposition is that it provides a quantitative definition of coherent structures as well as an unambiguous measure of their contribution to second-order turbulence statistics. The dominant eddy is defined to be that eigenfunction of the two-point correlation tensor associated with the largest eigenvalue (recall that the energy contributed by each eigenfunction is equal to its eigenvalue). This is an ideal application of simulation data bases because of the large magnitude of the required input data. Laboratory measurement of the full two-point correlation tensor is at best a tedious task. Application to both large-eddy- and direct-simulation data showed that the dominant eddy is indeed energetic and makes a significant contribution to turbulence production. As expected, the series expansion of turbulence stresses in terms of the eigenfunctions converges faster in the *lower-Reynolds-number* case (direct simulation).

In the directions of flow homogeneity, this expansion is combined with the shot-noise expansion to yield the characteristic eddy that is "sprinkled" in the flow. Prescription of the sprinkling function represents an ad-hoc input to an otherwise non-prejudicial technique. The shape of the eddy is directly related to the nature of the sprinkling function. Given a physically-realistic stochastic sprinkling function, the characteristic eddy can be obtained to within a phase factor. The phase information cannot be obtained from second-order statistics, so must be recovered from third-order statistics (Lumley 1981). Recently, Moin computed the bispectrum of the coefficient of the dominant eigenfunction in the velocity expansion. The bispectrum was used to determine the phase angle, allowing the characteristic eddy to be constructed. The contours of vertical velocity and the streamlines in the wall-layer corresponding to this structure are shown in Fig. 16. The streamlines depict intense high-speed fluid impinging on the wall. The return motion with positive vertical velocity is significantly less intense and more diffuse. The corresponding velocity vectors reveal a pair of relatively weak streamwise vortices 75 wall units apart and centered at $y^+ \approx 33$. However, the dominant structure appears to be the impingement flow. The intensity of the impinging flow rules out a causal relationship with the vortices. Thus, the dominant wall layer structure as determined from the characteristic-eddy decomposition appears to resemble an impingement flow rather than a pair of counterrotating vortices. Extension of the decomposition domain to larger y^+ values does not change this picture.

It is interesting to compare the dominant eddy from the characteristic-eddy decomposition to the instantaneous contour plots in Fig. 3. The instantaneous patterns generally indicate adjacent regions of fluid moving towards and away from the wall, although in some cases there are three adjacent regions, the two outside sections with one sign of v and the inner region with the opposite sign. The resemblance of these latter structures to the dominant eddy from the characteristic-eddy decomposition is probably due to the requirement of statistical symmetry of the normal and streamwise components of the eigenfunctions in the z direction. The statistical symmetry requirements preclude the detection of structures that may be present in the flow but do not satisfy the symmetry. To emphasize the v component of the velocity rather than turbulent kinetic energy, $(\overline{u^2} + \overline{v^2} + \overline{w^2})$, we have also found the eigenfunctions of the two-point correlation of the normal velocity component, $R_{vv}(y, y', z)$. The v contours of the resulting dominant eigenfunction are very similar to those in Fig. 16a.

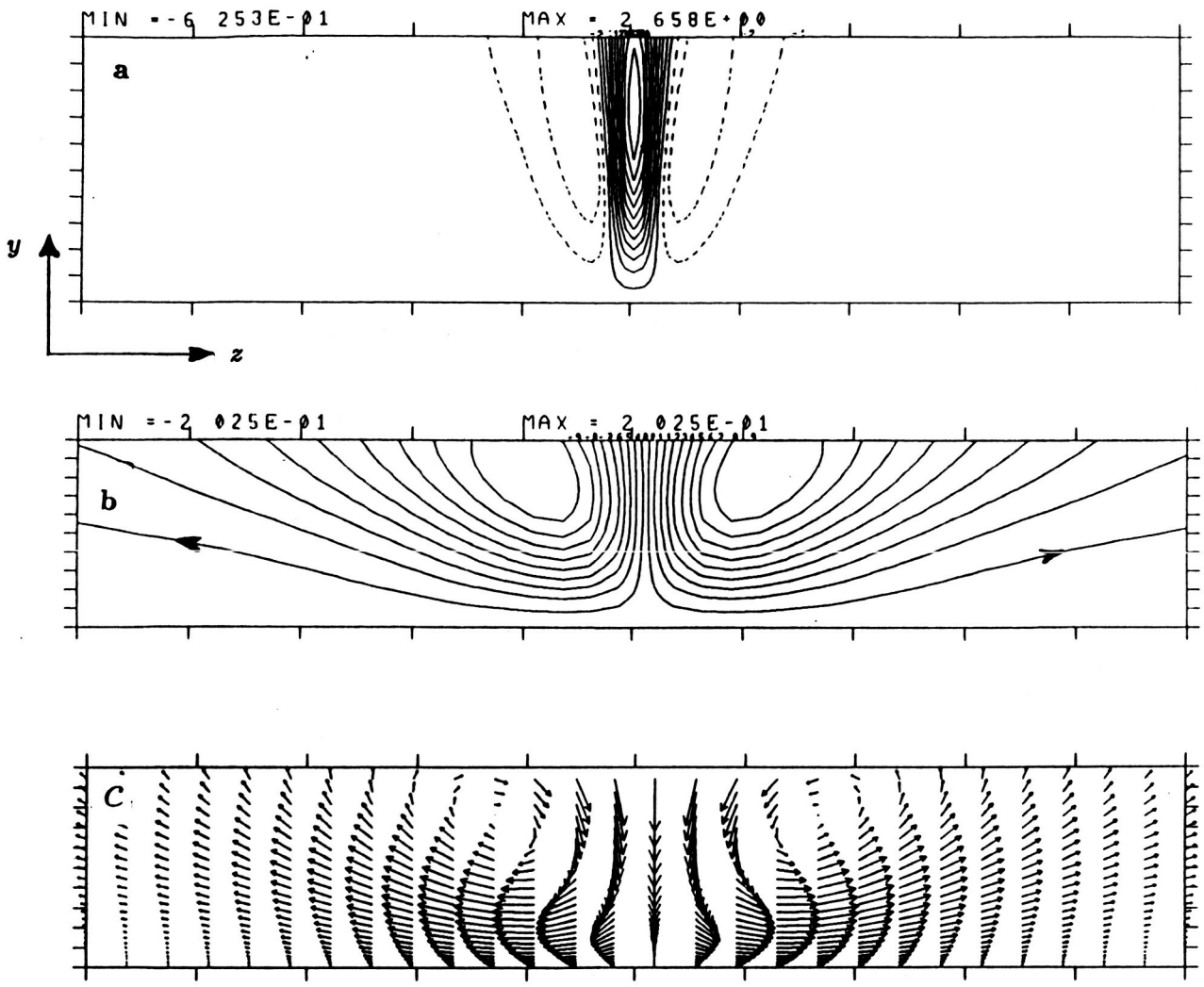

Figure 16. Dominant eddy from the characteristic-eddy decomposition using a low-Reynolds-number direct simulation. In the y direction, the figures extend from the wall to $y^+ = 40$. (a) Contours of v. Positive values (flow away from the wall) are indicated by dashed lines. (b) streamlines. (c) velocity vectors.

5.1 Stochastic estimation of conditional eddies

Recently, the homogeneous-shear-flow data base was used to evaluate the Stochastic Estimation Theory (Adrian 1979) used for detection of organized structures that satisfy certain conditions at a point. Given an ensemble of realizations of a flow, the problem is to find the *average* behavior of the velocity field near the points $\mathbf{x}$ at which prescribed conditions on the field are met. Given the conditions, $\mathbf{E}(\mathbf{x})$, at point $\mathbf{x}$, an estimate of $\mathbf{u}(\mathbf{x}+\mathbf{r})$ is sought. This estimate is the conditional eddy, $< \mathbf{u}(\mathbf{x}+\mathbf{r})|\mathbf{E}(\mathbf{x}) >$. The aforementioned problem statement describes the objectives in standard conditional-sampling studies. The VITA technique of Blackwelder &

Kaplan (1976), for example, is a popular conditional-sampling scheme used to detect bursting events and associated organized structures in turbulent boundary layers. The main criticism of conditional averaging and the interpretation of its results is that the prescribed conditions are usually subjective and therefore the significance of the detected structures may be questionable. In addition, experiments must be repeated whenever new conditions are imposed. In this section, these issues will be addressed.

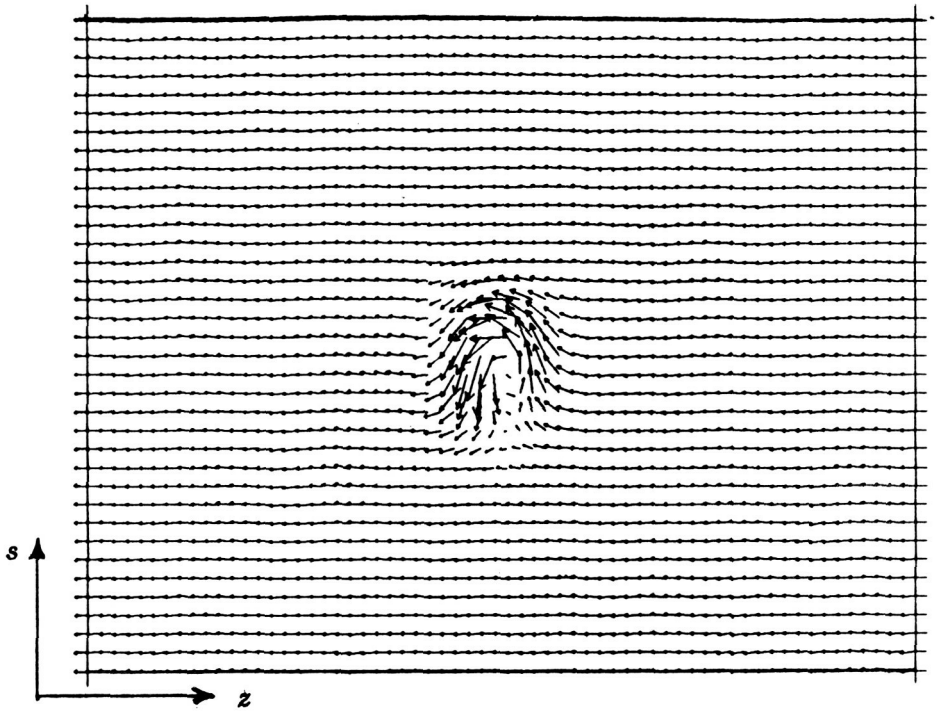

Figure 17. Projection of the vorticity vectors of the conditional eddy corresponding to conditions at point (*) in Fig. 12.

In stochastic estimation, one seeks an approximation of the conditional eddy, $< \mathbf{u}(\mathbf{x}+\mathbf{r})|\mathbf{E}(\mathbf{x}) >$, in terms of the data $\mathbf{E}(\mathbf{x})$. The simplest approximation is the linear representation

$$\hat{u}_i(\mathbf{x}+\mathbf{r}) = L_{ij}(\mathbf{r})E_j(\mathbf{x}) \tag{1}$$

where L_{ij} is the unknown coefficient to be determined. The relevant condition at $\mathbf{x}$ is the velocity vector v_i, or the prescription of both the velocity vector and the deformation tensor $d_{ij} \equiv \frac{\partial v_i}{\partial x_j}$. In the latter case, for homogeneous flows, Eq. (1) can be generalized to

$$\hat{u}_i(\mathbf{x}+\mathbf{r}) = A_{ij}(\mathbf{r})\ v_j(\mathbf{x}) + B_{ijk}(\mathbf{r})\ d_{jk}(\mathbf{x}) \tag{2}$$

The coefficients A_{ij} and B_{ijk} are obtained by minimizing the mean-square error

$$e_l = < \left(u_l(\mathbf{x}+\mathbf{r}) - \hat{u}_l(\mathbf{x}+\mathbf{r})\right)^2 >$$

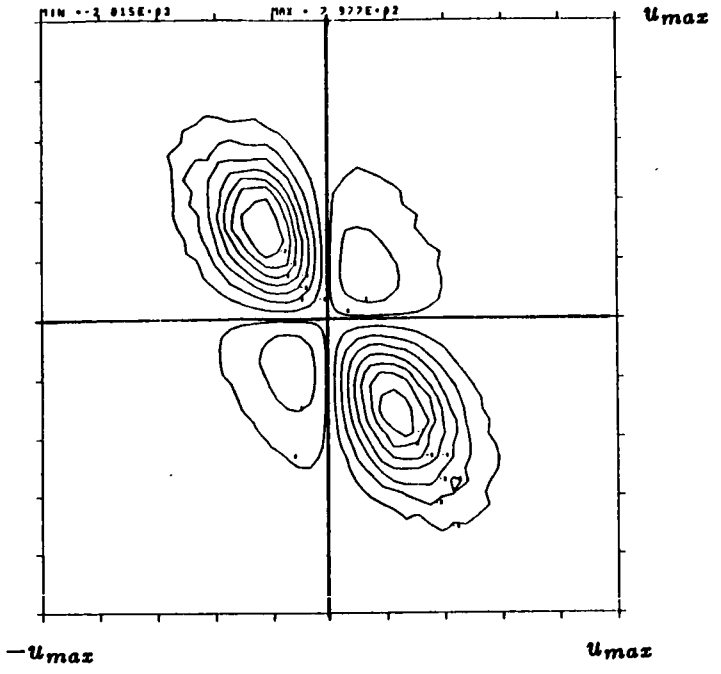

Figure 18. Weighted joint velocity probability density for homogeneous shear flow.

We thus require

$$\frac{\partial e_l}{\partial A_{ij}} = 0 \tag{3a}$$

and

$$\frac{\partial e_l}{\partial B_{ijk}} = 0 \tag{3b}$$

for $i,j,k,l = 1,2,3$. Equation 3 leads to the following system of algebraic equations for the unknowns A_{ij} and B_{ijk}

$$A_{ij}(\mathbf{r})R_{lj}(0) + B_{ijk}(\mathbf{r})R_{lj,k}(0) = R_{li}(\mathbf{r})$$

$$A_{ij}(\mathbf{r})R_{lj,m}(0) - B_{ijk}(\mathbf{r})R_{lj,km}(0) = -R_{li,m}(\mathbf{r})$$

where $R_{ij}(\mathbf{r}) \equiv < u_i(\mathbf{x})u_j(\mathbf{x}+\mathbf{r}) >$ is the two-point correlation tensor. Inclusion of the continuity equation leaves an 11×11 system of equations for each i and every $\mathbf{r}$. The matrix elements are independent of i and $\mathbf{r}$, and the matrix is inverted only once. Note that the coefficients A_{ij} and B_{ijk} are functions only of the two-point correlation tensor (and its derivatives). Thus, for each flow, the two-point correlation tensor must be computed, and from it we can obtain the coefficients in Eq. (2). The conditional eddies can then be obtained by simply using the corresponding conditions in Eq. (2). *Note that we have shown that the conditional eddy, at least to a first-order approximation, can be obtained from the two-point correlation tensor, which is a long-time-averaged statistical correlation.*

The conditional eddy satisfies the continuity equation, matches the data at point $\mathbf{x}$, and decays to zero far away from $\mathbf{x}$. The mean-square error of the representation,

$e_l(\mathbf{r})$, ranges from zero at $\mathbf{x}$ to its maximum value, $\overline{u_l^2}$, at large distances from $\mathbf{x}$. The conditional velocity field has a number of other useful properties (see Adrian & Moin 1987 for details).

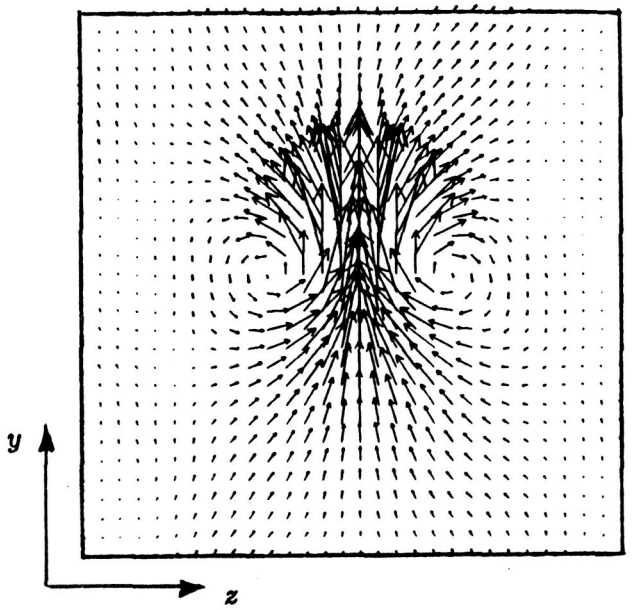

Figure 19. Velocity vectors of the conditional eddy corresponding to conditions at the second-quadrant peak of the probability-density function in homogeneous shear flow.

The estimation algorithm was applied to a velocity field in homogeneous turbulent shear flow generated by direct numerical simulation (Adrian & Moin 1987). To verify the accuracy of the algorithm the exact v_j and d_{jk} data (conditions) at a point in the instantaneous field were used as input into Eq. (2). The resulting conditional eddy corresponding to the data at the point marked (*) in Fig. 12 is shown in Fig. 17. Note that point (*) is located on the tip of a hairpin vortex in the instantaneous field. Figure 17 shows the projection of vorticity vectors onto a plane inclined at 45° to the flow direction and passing through the data point. The agreement of the detected structure and the structure in the neighborhood of the point (*) in the instantaneous field is good. The conditional eddy resembles a compact hairpin vortex. As expected the algorithm is most accurate near the detection point (at the center of the figure). Portions of the hairpin legs far away from $\mathbf{x}$ are not captured.

The issue of objectivity in the selection of the conditions is addressed by using the probability-density function of all possible conditions. The probability-density function provides information about the frequency of occurrence of the conditions, and can be used to select the conditions corresponding to events of interest. For example, if we seek structures associated with regions of high turbulence production, the appropriate conditions correspond to the maximum of the weighted probability-density function $uvP(\mathbf{u}, d)$. This weighted probability-density function has also been

measured and analyzed by Perry & Hoffmann (1976) and others. The Reynolds shear stress is given by

$$\overline{uv} = \int uv\ P(\mathbf{u}, d)\ d\mathbf{u}\ d\mathbf{d}$$

where $\mathbf{d}$ is the deformation tensor.

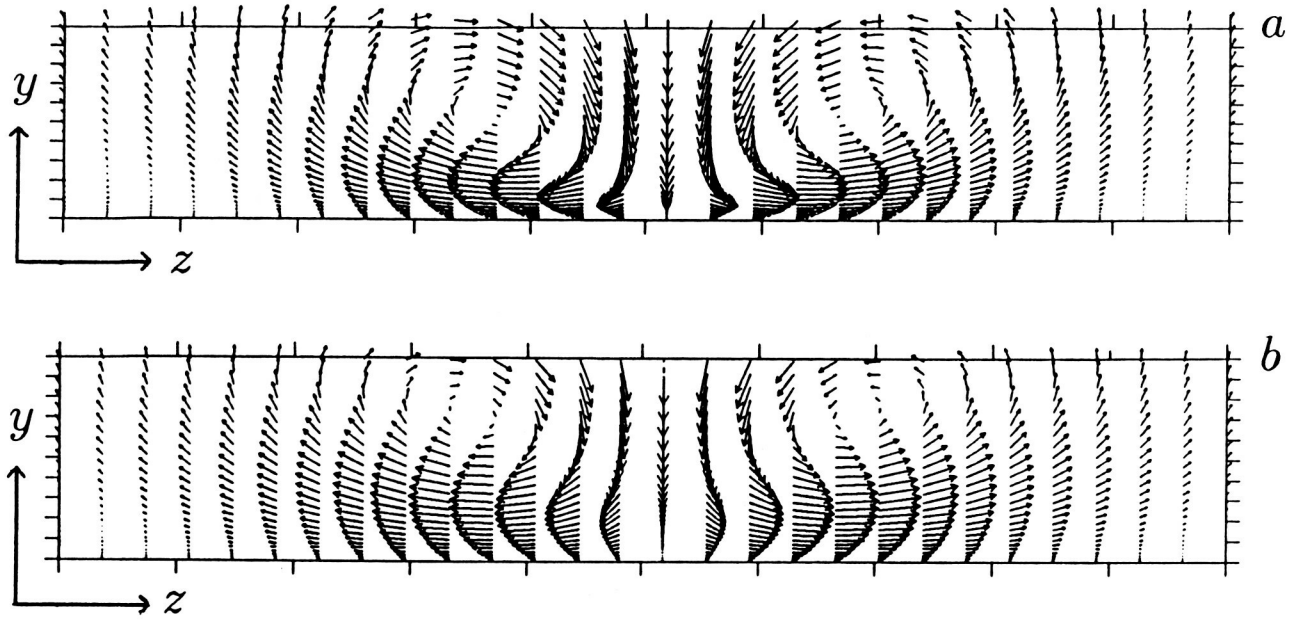

Figure 20. Velocity vectors of the conditional eddy corresponding to conditions at the fourth-quadrant peak of the probability-density function in channel flow. (a) $y^+ \approx 5$, (b) $y^+ \approx 19$.

The weighted joint probability-density function, $uvP(u,v)$, is shown in Fig. 18 for the homogeneous-shear-flow field used in the present study. We find that at the point(s) of maximum $uvP(\mathbf{u}, d)$, $\mathbf{d} = 0$, $w = 0$. The conditional eddy corresponding to the u and v values of the peak in the second quadrant in Fig. 18 was computed. The velocity vectors in a (y, z) plane upstream of the detection point are shown in Fig. 19. This cross-section of the conditional eddy displays a pair of roller eddies with intense induced vertical velocity. Examination of other (y, z) cross-sections indicate that the centers of the rollers are located along lines inclined at 45° to the flow direction. The corresponding vortex lines display a hairpin-shaped structure.

The stochastic-estimation algorithm was also applied to the channel flow (Moin, Adrian & Kim 1987). A two-dimensional variant of the algorithm ($y - z$ planes) with only velocity conditions specified was considered. Thus equation (2) was replaced by

$$\hat{u}_i(y', z + r_z) = L_{ij}(y, y', r_z) v_j(y, z)$$

where (y, z) is the fixed point where the data (condition) is satisfied. Conditions corresponding to the peak in the fourth quadrant of the weighted joint velocity probability

distribution in the channel flow at $y^+ \approx 5$ and $y^+ \approx 19$ resulted in the conditional eddies shown in Figs. 20a and 20b, respectively. Observe the strong similarity between these figures (particularly Fig. 20b for which the detection point is at the center of the domain) and Fig. 16c.

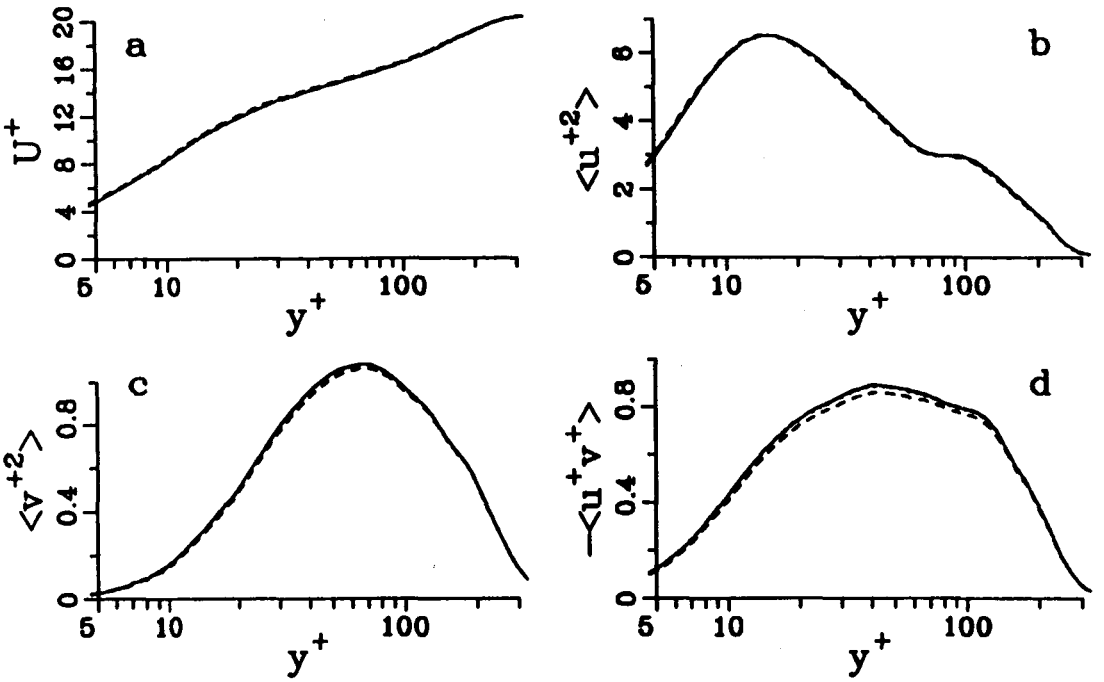

Figure 21. Measured quantities in a boundary layer, using basic probe. —— exact values; — — — using (5), but with w and k_1 set to 0; - - - - using (5), w not set to 0; $\cdots$ using (5), $k_1^2 = 0.04$

6. Evaluation of hot-wire response in a turbulent boundary layer

One of the promising applications of numerical data bases is to help design laboratory probes. In this section a fairly complete model of an X-wire probe is considered, and its response is computed using a turbulent-boundary-layer flow field obtained by direct simulation. This allows one to estimate quantitatively the accuracy of X-wire measurements, how this accuracy depends on the distance from the wall, and also to isolate the various sources of error, e. g., axial cooling of the wires and neglect of the velocity component normal to the plane of the wires (Li, Henbest & Perry 1986 for a discussion of these effects). All of these errors depend on the joint probability distribution of u, v, and w.

An X-wire model and the value of the constants were provided by Professor A. E. Perry (personal communication, see also Perry 1982). A slightly simplified version of his model is used here. The probe is used to measure u and v; its two wires are in an $x - y$ plane. Let $\mathbf{s}_1$ and $\mathbf{s}_2$ be unit vectors in the direction of the two wires.

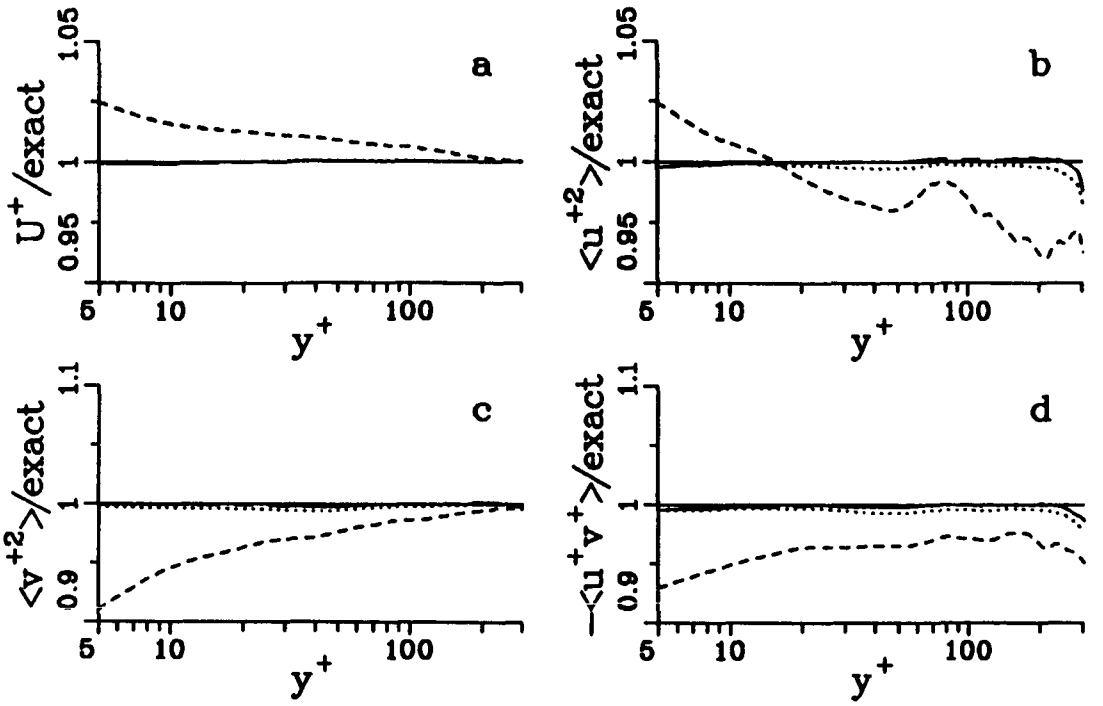

Figure 22. Relative errors in measured quantities, using basic probe. —— exact values; — — — using (5), but with w and k_1 set to 0; - - - - using (5), w not set to 0; $\cdots$ using (5), $k_1^2 = 0.04$

By convention, their y-component is positive. Let $\mathbf{u}$ be the velocity vector. The "effective cooling velocity" U_{e1} on the first wire is given by

$$U_{e1} \equiv \sqrt{||\mathbf{u} \times \mathbf{s}_1||^2 + k_1^2(\mathbf{u} \cdot \mathbf{s}_1)^2} \tag{4}$$

with an equivalent formula for the second wire. The first term represents the primary contribution, cooling by the component of velocity orthogonal to the wire, while the second term represents axial cooling of the wire. The value of k_1^2 is taken as 0.04.

One has access to only two cooling velocities, U_{e1} and U_{e2}, which are always positive. Thus it is not possible to measure w, or to obtain the signs of both u and v. The standard procedure is to assume that u is positive and that v is much smaller than u, and to ignore w. Equation (4) is then linearized with v/u as the small parameter. The result is

$$U_{e1} \approx a_1 \, s_{1y} \, u - b_1 \, s_{1x} \, v, \qquad U_{e2} \approx a_1 \, s_{2y} \, u - b_1 \, s_{2x} \, v. \tag{5}$$

The factors a_1 and b_1 are associated with axial cooling: $a_1 \equiv \sqrt{1 + (k_1 s_{1x}/s_{1y})^2}$ and $b_1 \equiv (1 - k_1^2)/a_1$. Equation (5) is a linear system and can be inverted easily to obtain u and v.

A typical experimental procedure is to obtain a linear relation of the type given by (5) by calibration in a known flow, again assuming $v << u$. This eliminates the need to know $\mathbf{s}_1$ and $\mathbf{s}_2$ to a high accuracy; the calibration may also account for effects

ignored by the model that led to (5), such as interference with the prongs that are holding the wires.

The quantities that were "measured" are the mean velocity U and the three Reynolds stresses $< u^2 >$, $< v^2 >$, and $- < uv >$. The angle between the wires, α, is commonly 90°, but larger angles such as 120° are advocated by Perry (1982). Computations will be done with $\alpha = 90°$ ($s_{1x} = s_{1y} = -s_{2x} = s_{2y} = \sqrt{1/2}$) and $\alpha = 120°$ ($s_{1x} = -s_{2x} = 1/2$, $s_{1y} = s_{2y} = \sqrt{3/4}$). Another improvement is obtained by "flying" the probe, which makes the assumption $v << u$ more valid. Also, the wires cannot be in the same $x - y$ plane; the effect of the distance d between them will be investigated.

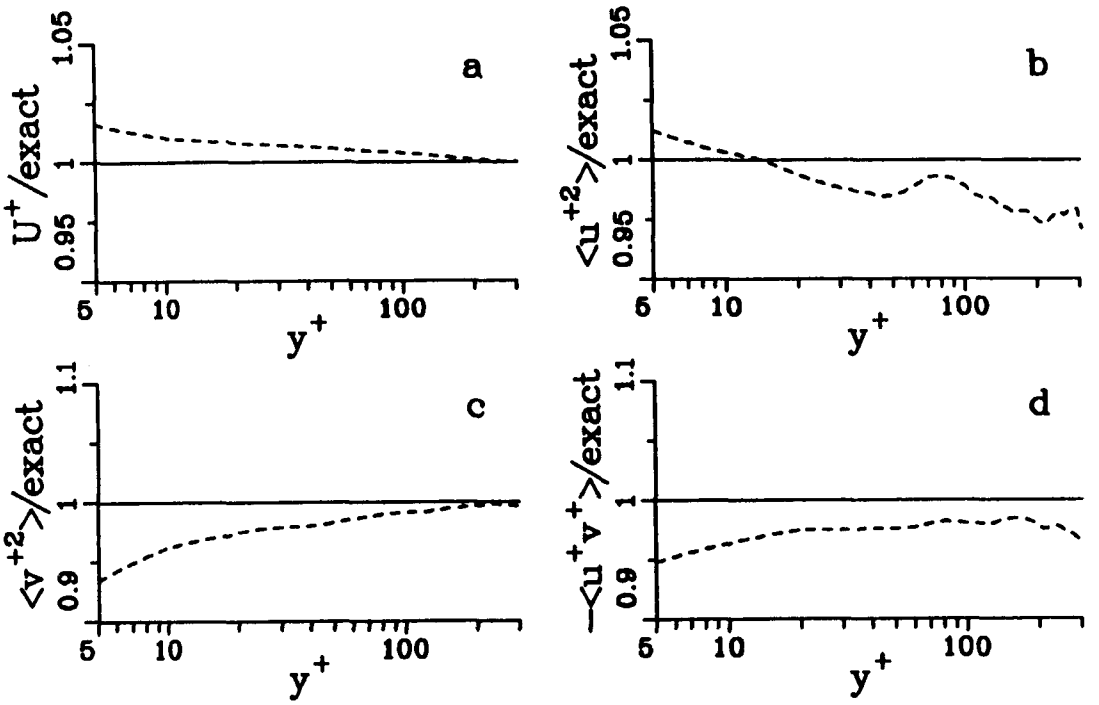

Figure 23. Relative errors in measured quantities, with $\alpha = 120°$. —— exact values; ---- measured values (w not set to 0).

We can test the sources of error one by one. The assumption $u > 0$ cannot lead to appreciable errors in the present flow. The simulation results indicate that (at least at $R_\theta = 670$ and with zero pressure gradient) it is extremely rare for u to become negative. The "basic" probe ($\alpha = 90°$, $d = 0$, no flying) is considered first. We first isolate the effects of the linearization that led to (5). This is accomplished by artificially setting the w component to 0 when computing U_{e1} and U_{e2}. The axial-cooling constant k_1 is also set to 0. In Fig. 21 the actual values of the velocities are shown, which makes the errors difficult to distinguish; in Fig. 22 and subsequent figures the ratio of the measured values to the exact values is plotted to emphasize the relative errors. Figure 22 shows that the errors caused by the linearization alone are small, at most 1%. Thus a nonlinear (in terms of v/u) calibration procedure seems unwarranted, at least in the present flow.

The errors caused by axial cooling are computed next; w is still set to 0 in (4) but $k_1^2 = 0.04$. We find that the axial-cooling effects are very well represented by the a_1 and b_1 factors, as shown in Fig. 22. On the other hand the spanwise velocity component has a strong effect. When w is not artificially set to 0, large errors appear, of the order of 5% even for U; this is due to the nonlinearities in (4). The relative errors are roughly twice as large for v as they are for u. Unfortunately this would be difficult to compensate for without resorting to assumptions about the correlation between u, v, and $|w|$.

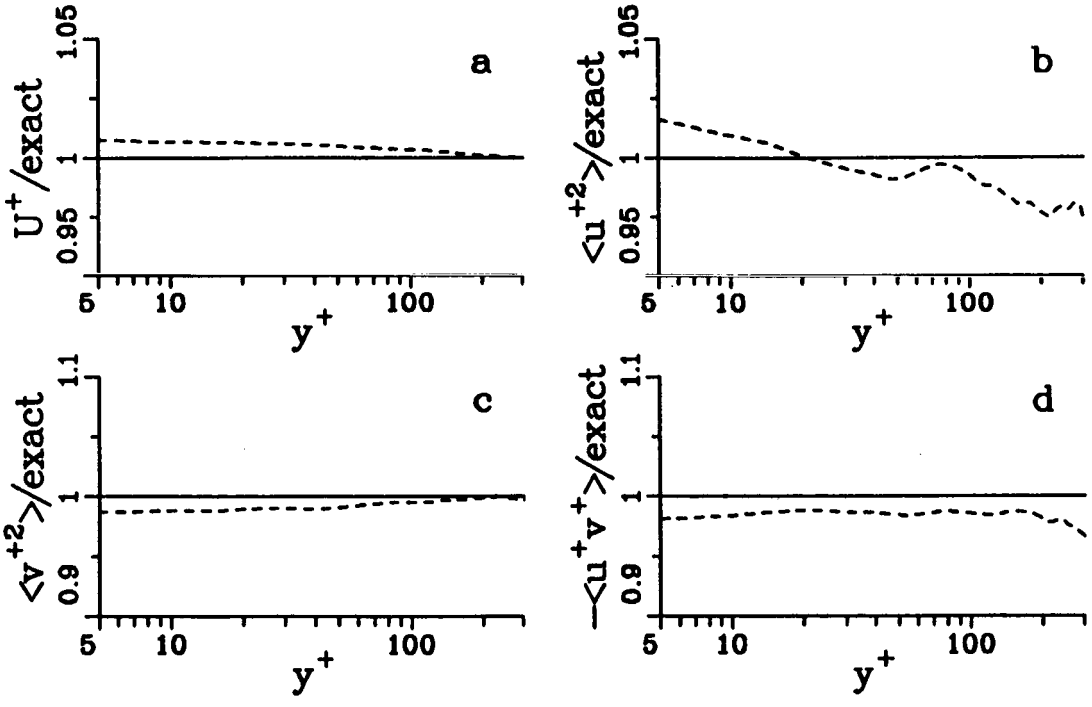

Figure 24. Relative errors in measured quantities, with probe flying at $U_\infty/2$. —— exact values; ---- measured values (w not set to 0).

Figure 23 shows the results with wires at 120° and the w component is not set to 0. One finds that the error is reduced in all components by 25 to 50%. Thus an increase in the angle is helpful, but in practice one is also concerned about the signal-to-noise ratio, which decreases as α increases (in the limit of a 180° angle, Eq. (5) becomes singular). Figure 24 shows that flying the probe is very effective. The probe is translating upstream at half of the freestream velocity. The largest error is now only about 2%. As the flying velocity increases, the ratios v/u and w/u both tend to 0 and (5) becomes more accurate; on the other hand, the signal-to-noise ratio again decreases as the flying velocity increases.

In Fig. 25 the effect of a separation between the two wires is shown. One of the wires is displaced by one wall unit in the z direction, and w and k_1 are again set to 0. The effect is very strong, even with such a small separation. The reason is that when Eq. (5) is inverted v is to leading order given by the difference between U_{e1} and U_{e2}. When the two wires are not in exactly the same place, $U_{e1} - U_{e2}$ is artificially

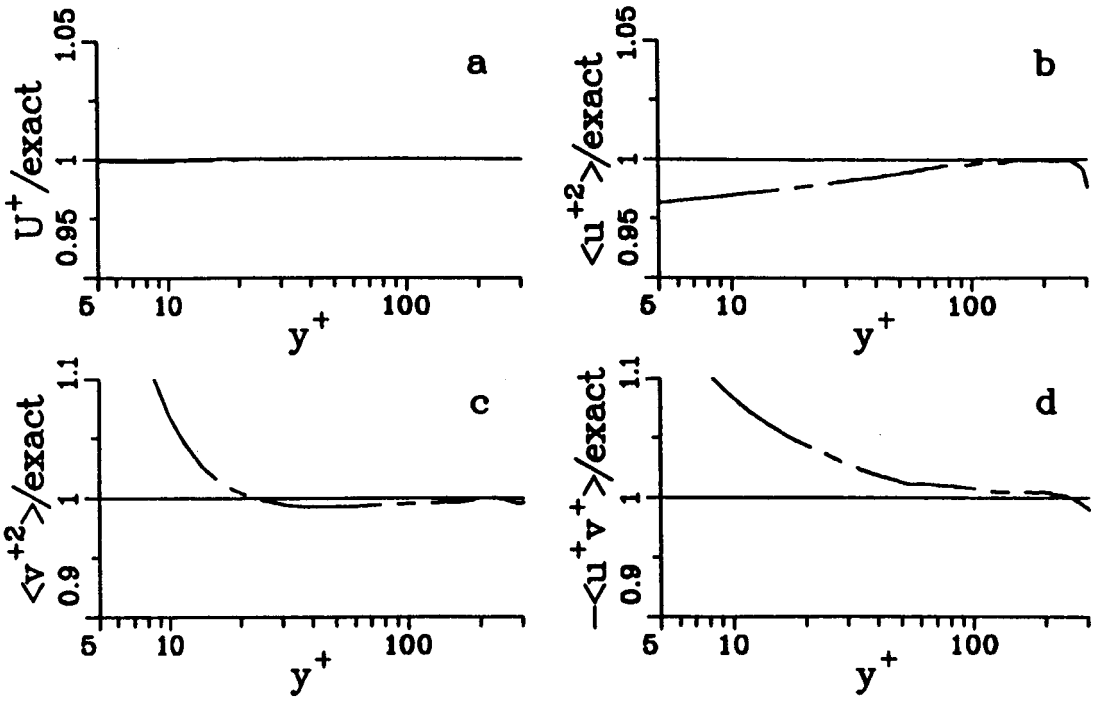

Figure 25. Relative errors in measured quantities, with wires one wall unit apart. —— exact values; — - - - measured values (w set to 0).

enhanced, leading to a large overestimation of v. The reason why existing probes, for which d^+ is often 10 or more, work is that their finite-length wires filter out the small-scale motion which is predominantly responsible for the error. Obtaining accurate measurements may be a matter of balance between the dimensions of the probe, as well as a reduction of these dimensions.

Overall, the results of the X-wire study show that the errors caused by the neglect of the spanwise component are much larger than those caused by linearized calibration or axial cooling. Increasing the wire angle to 120° and especially flying the probe improve the accuracy significantly. In the log layer, the relative errors are found to be of the order of a few percent. The errors caused by finite-length wires, which have not yet been computed, may be at least as large, depending on the value of y^+.

7. Application to Turbulence Modeling

The use of simulation data for design and testing of phenomenological turbulence models began with the early large-eddy simulations (Moin, Reynolds & Ferziger 1978). Because of the coarse meshes and sub-grid-scale-model errors in these early simulations, the results could only be used qualitatively. The data from Rogallo's (1981) direct simulation of homogeneous turbulent flows was the first to be used for comprehensive evaluation of turbulence models.

Moser & Moin (1984) computed the Reynolds-stress budget in curved channel flow. By comparing the concave and convex sides of the channel, it was found that curvature

had only a small effect on the terms in the balance of the normal stresses, but had a significant effect on the Reynolds-shear-stress budget. Recently, the Reynolds-stress budget in plane channel flow as well as the terms in the equation for turbulent-kinetic-energy dissipation rate have been computed (Mansour, Kim & Moin 1986) and the results were compared with the phenomenological models.

Simulation data bases that contain passive scalar fields are also being used in model development. Rogers, Moin & Reynolds (1986) computed several homogeneous shear flows with passive scalar contaminant at different molecular Prandtl numbers and with mean scalar gradients along all three coordinate directions. They found that scalar eddy-diffusivity formulations that assume that the scalar flux is aligned with the mean scalar gradient are inadequate. A physical explanation for this inadequacy was based on coherent structures found in the flow. It was found that hairpin vortices control the observed turbulent scalar flux. A gradient-transport model employing a turbulent diffusivity *tensor* was found to model the simulation results to within 20%. In addition, it was shown that the turbulent Prandtl number was a strong function of the direction of the mean scalar gradient (relative to the direction of the mean shear) and a weak function of the molecular Prandtl number. The dependence on the molecular Prandtl number was also confirmed in channel-flow simulations with scalar contaminants.

8. Summary

Several examples were provided in which the use of simulation data bases has led to enhanced phenomenological turbulence modeling and to a better physical understanding of turbulent flows and of their measurement.

In wall-bounded flows, direct numerical simulations and recent measurements appear to have converged on accurate boundary values for the *rms* shear-stress fluctuations and the turbulent-kinetic-energy dissipation rate at the wall. The early measurements of these quantities had yielded significantly lower values.

In the vicinity of the wall, the normal velocity component is highly intermittent and dominated by adjacent regions of fluid moving away from and towards the wall. Single vortices with a streamwise extent of 100 to 200 wall units appear to be the fundamental structures associated with regions of high turbulence production. These vortices sometimes occur in pairs constituting the legs of a horseshoe vortex.

The flow structures were correlated with shear-stress and pressure patterns at the wall. Convergence of the friction lines is associated with upward motion and low pressure near the wall, and conversely the lines diverge in regions of downward motion and high pressure. The low-pressure regions tend to be elongated and to coincide with the cores of vortices, whereas the high-pressure regions are more circular and extend farther in the y direction.

It was found that the organized structures in homogeneous shear flow are similar to those in turbulent boundary layers. In the cases considered, similarity of organized structures results in similarity of statistical correlations as well. The data from homogeneous shear flows with a passive scalar field were used in design and testing of phenomenological models for scalar flux. It was shown that eddy-diffusivity models,

which assume that the scalar flux is aligned with the mean scalar gradient, are inadequate. A physical explanation for the observed direction of the turbulent scalar flux was provided, based on hairpin vortices found in the flow.

The use of statistical correlations for the detection and analysis of organized structures was discussed. The shape of the dominant eddy from the characteristic-eddy decomposition is affected by the stochastic-eddy sprinkling function in the directions of flow homogeneity and by the inherent statistical symmetries of the eigenfunctions. The stochastic-estimation algorithm was used to approximate conditional eddies in homogeneous turbulent shear flow and in channel flow. A probability-density function provided conditions corresponding to high-Reynolds-shear-stress producing events. In homogeneous shear flow the corresponding conditional eddy is a hairpin vortex. In channel flow, there is a strong similarity between the dominant eddy in characteristic-eddy decomposition and the conditional eddy predicted by stochastic estimation.

A study of the response of an X-wire probe in a turbulent boundary layer was presented. The magnitude of the errors that should be expected near the wall was computed. These errors are predominantly caused by the neglect of the spanwise velocity component, and the study confirmed that they can be reduced by setting the angle between the wires to 120° or "flying" the probe.

Acknowledgments. The authors thank Professor A. Perry (University of Melbourne) for several suggestions (see sections 3.1 and 6) and Dr. R. Moser (NASA Ames Research Center) for reviewing the manuscript.

References

ADRIAN, R. J. 1979 Conditional eddies in isotropic turbulence. *Phys. Fluids* **22**, 2065.

ADRIAN, R. J. & MOIN, P. 1987 Stochastic estimation of organized turbulent structures: homogeneous shear flow. Submitted to *J. Fluid Mech.*

ALFREDSSON, P. H., JOHANSSON, A. V., HARITONIDIS, J. & ECKELMANN, H. 1987 On the fluctuating wall shear stress and the velocity field in the viscous sublayer. Submitted to *J. Fluid Mech.*

BLACKWELDER, R. F. & KAPLAN, R. E. 1979 On the structure of the turbulent boundary layer. *J. Fluid Mech.* **76**, 89.

HANRATTY, T. J., CHORN, L. G. & HATZIAVRAMIDIS, D. T. 1977 Turbulent fluctuations in the viscous wall region for Newtonian and drag reducing fluids. *Phys. Fluids* **20**, S112.

HORNUNG, H. & PERRY, A. E. 1984 Some aspects of three-dimensional separation, Part 1: streamsurface bifurcations. *Z. Flugwiss. Weltraumforsch.* Vol. 8, No. 2, 77.

KIM, J. & MOIN, P. 1986a The structure of the vorticity field in turbulent channel flow. Part 2. Study of ensemble-averaged fields. *J. Fluid Mech.* **162**, 339.

KIM, J. & MOIN, P. 1986b Flow structures responsible for the bursting process. Bulletin of the American Physical Society, **31**, 10, 1716.

KIM, J., MOIN, P. & MOSER, R. D. 1987 Turbulence statistics in fully-developed channel flow at low Reynolds number. *J. Fluid Mech.* **177**, 133.

KLINE, S. J., REYNOLDS, W. C., SCHRAUB, F. A., & RUNSTADLER, P. W. 1967 The structure of turbulent boundary layers. *J. Fluid Mech.* **30**, 741.

KREPLIN, H. & ECKELMANN, H. 1979 Behavior of the three fluctuating velocity components in the wall region of a turbulent channel flow. *Phys. Fluids* **22**, 1233.

LEE, M. J., KIM, J. & MOIN, P. 1986 Effect of high shear-rate on the structure of turbulence. Bulletin of the American Physical Society, **31**, 10, 1725.

LI, J. D., HENBEST, S. M. & PERRY, A. E. 1986 The difficulties in the measurements of Reynolds stresses in smooth- and rough-wall turbulent boundary layers. Proceedings of the 9^{th} Australasian Fluid Mechanics Conference, Auckland, New Zealand, Dec. 8-12, 1986.

LUMLEY, J. L. 1967 The structure of inhomogeneous turbulent flows. In *Atmospheric Turbulence and Radio Wave Propagation*, ed. A. M. Yaglom & V. I. Tatarsky, pp. 166. NAUKA, Moscow.

LUMLEY, J. L. 1981 Coherent structures in turbulence. in *Transition and Turbulence*, ed. R.E. Meyer, Academic Press, New York, 215.

MANSOUR, N. N., KIM, J. & MOIN, P. 1986 The dissipation rate of the Reynolds-stress tensor. Bulletin of the American Physical Society, **31**, 10, 1725.

MOIN, P. 1984 Probing turbulence via large-eddy simulation. *AIAA Paper 84-0174.*

MOIN, P., ADRIAN, R. J., & KIM, J. 1987 Stochastic estimation of conditional eddies in turbulent channel flow. Proceedings of the 6^{th} Symposium on turbulent shear flows, Toulouse, France, Sept. 7-9, 1987.

MOIN, P. & KIM, J. 1982 Numerical investigation of turbulent channel flow. *J. Fluid Mech.* **118**, 341.

MOIN, P. & KIM, J. 1985 The structure of the vorticity field in turbulent channel flow. Part 1. Analysis of instantaneous fields and statistical correlations. *J. Fluid Mech.* **155**, 441.

MOIN, P., REYNOLDS, W. C. & FERZIGER, J. H. 1978 Large-eddy simulation of incompressible turbulent channel flow. *Report TF-12*, Department Mechanical Engineering, Stanford Univ., Stanford, Calif.

MOSER, R. D. & MOIN, P. 1984 Direct numerical simulation of curved turbulent channel flow. *NASA TM 85974.* Also, *J. Fluid Mech.* **175** (1987), 479.

NAQWI, A. A. & REYNOLDS, W. C. 1987 Dual cylindrical wave laser-doppler method for measurement of skin friction in fluid flow. *Report TF-28*, Department Mechanical Engineering, Stanford Univ., Stanford, Calif.

PERRY, A. E. 1982 *Hot-wire anemometry.* Clarendon, Oxford.

PERRY, A. E. & HOFFMANN, P. H. 1976 An experimental study of turbulent convective heat transfer from a flat plate. *J. Fluid Mech.* **77**, 355.

PERRY, A. E. & HORNUNG, H. 1984 Some aspects of three-dimensional separation, Part 2: vortex skeletons. *Z. Flugwiss. Weltraumforsch.* Vol. 8, No. 3, 155.

ROGALLO, R., S. 1981 Numerical experiments in homogeneous turbulence *NASA TM-81315.*

ROGERS, M. M. & MOIN, P. 1987 The structure of the vorticity field in homogeneous turbulent flows. *J. Fluid Mech.* **176**, 33.

ROGERS, M. M., MOIN, P. & REYNOLDS, W. C. 1986 The structure and modeling of the hydrodynamic and passive scalar fields in homogeneous turbulent shear flow. *Dept. Mech. Engng. Rep.* TF-25, Stanford Univer., Stanford, Calif.

SPALART, P. R. 1986 Direct simulation of a turbulent boundary layer up to R_θ = 1410. NASA TM-89407. Also to appear in *J. Fluid Mech.*

THEODORSEN, T. 1952 Mechanism of turbulence. Proc. 2nd Midwestern Conference on Fluid Mech. Ohio State Univ., Columbus, Ohio.

1. Report No.	2. Government Accession No.	3. Recipient's Catalog No.
NASA TM 100022		

4. Title and Subtitle	5. Report Date
Contributions of Numerical Simulation Data Bases to the Physics, Modeling, and Measurement of turbulence	September 1987
	6. Performing Organization Code
7. Author(s)	8. Performing Organization Report No.
Parviz Moin and Philippe R. Spalart	A-87276
	10. Work Unit No.
9. Performing Organization Name and Address	505-60
Ames Research Center Moffett Field, CA 94035	11. Contract or Grant No.
	13. Type of Report and Period Covered
12. Sponsoring Agency Name and Address	Technical Memorandum
National Aeronautics and Space Administration Washington, DC 20546-0001	14. Sponsoring Agency Code

15. Supplementary Notes

Point of Contact: Philippe R. Spalart, Ames Research Center, M/S 202A-1, Moffett Field, CA 94035
(415)694-4734 or FTS 464-4734

16. Abstract

The use of simulation data bases for the detailed examination of turbulent flows has proved to be an effective research tool. In the past, studies of the structure of turbulence have been hampered by the limited number of probes and the impossibility of measuring all the desired quantities. Also, flow visualizations are confined to the observation of passive markers with limited field of view and contamination caused by time-history effects. Computed flow fields are a new resource for turbulence research, providing all the instantaneous flow variables in three-dimensional space.

Simulation data bases also provide much-needed information for phenomenological turbulence modeling. Even for simple shear flows, most of the terms in the Reynolds-stress transport equations have not been measured experimentally. Three-dimensional velocity and pressure fields from direct simulations can be used to compute all the terms in the transport equations for the Reynolds stresses and the dissipation rate. However, only a few, geometrically-simple flows have been computed by direct numerical simulations, and the inventory of simulation fields does not fully address the current modeling needs in complex turbulent flows.

The availability of three-dimensional flow fields also poses challenges in developing new techniques for their analysis. Most current techniques do not take advantage of the vast amount of data at the researcher's disposal. They are often based on experimental methods, developed when limited data could be measured. Although some of these techniques are useful when comparing with experimental observations for code validation, new visualization and statistical techniques need to be developed to allow a comprehensive analysis of the simulation data.

In this paper we shall describe some of the techniques that have been used for the analysis of direct-simulation data bases in our studies of the mechanics of turbulent flows. We will use examples in which original contributions were made to the understanding of the physics of turbulent flows or to modeling efforts. These contributions have resulted from the availability of complete three-dimensional data.

17. Key Words (Suggested by Author(s))	18. Distribution Statement
Turbulence Numerical simulation	Unclassified – Unlimited Subject Category – 02

19. Security Classif. (of this report)	20. Security Classif. (of this page)	21. No. of Pages	22. Price*
Unclassified	Unclassified	30	A03

*For sale by the National Technical Information Service, Springfield, Virginia 22161